

Planck 2013 results. XIX. The integrated Sachs-Wolfe effect

Planck Collaboration: P. A. R. Ade⁸⁷, N. Aghanim⁶⁰, C. Armitage-Caplan⁹³, M. Arnaud⁷⁴, M. Ashdown^{71,6}, F. Atrio-Barandela¹⁸, J. Aumont⁶⁰, C. Baccigalupi⁸⁶, A. J. Banday^{97,9}, R. B. Barreiro⁶⁸, J. G. Bartlett^{1,69}, N. Bartolo³³, E. Battaner⁹⁹, K. Benabed^{61,95}, A. Benoît⁵⁸, A. Benoit-Lévy^{25,61,95}, J.-P. Bernard⁹, M. Bersanelli^{36,50}, P. Bielewicz^{97,9,86}, J. Bobin⁷⁴, J. J. Bock^{69,10}, A. Bonaldi⁷⁰, L. Bonavera⁶⁸, J. R. Bond⁸, J. Borrill^{13,90}, F. R. Bouchet^{61,95}, M. Bridges^{71,6,65}, M. Bucher¹, C. Burigana^{49,34}, R. C. Butler⁴⁹, J.-F. Cardoso^{75,1,61}, A. Catalano^{76,73}, A. Challinor^{65,71,11}, A. Chamballu^{74,15,60}, L.-Y. Chiang⁶⁴, H. C. Chiang^{28,7}, P. R. Christensen^{82,39}, S. Church⁹², D. L. Clements⁵⁶, S. Colombi^{61,95}, L. P. L. Colombo^{24,69}, F. Couchot⁷², A. Coulais⁷³, B. P. Crill^{69,83}, A. Curto^{6,68}, F. Cuttaia⁴⁹, L. Danese⁸⁶, R. D. Davies⁷⁰, R. J. Davis⁷⁰, P. de Bernardis³⁵, A. de Rosa⁴⁹, G. de Zotti^{46,86}, J. Delabrouille¹, J.-M. Delouis^{61,95}, F.-X. Désert⁵⁴, C. Dickinson⁷⁰, J. M. Diego⁶⁸, K. Dolag^{98,79}, H. Dole^{60,59}, S. Donzelli⁵⁰, O. Doré^{69,10}, M. Douspis⁶⁰, X. Dupac⁴¹, G. Efstathiou⁶⁵, T. A. Enßlin⁷⁹, H. K. Eriksen⁶⁶, J. Fergusson¹¹, F. Finelli^{49,51}, O. Forni^{97,9}, P. Fosalba⁶², M. Frailis⁴⁸, E. Franceschi⁴⁹, M. Frommert¹⁷, S. Galeotta⁴⁸, K. Ganga¹, R. T. Génova-Santos⁶⁷, M. Giard^{97,9}, G. Giardino⁴², Y. Giraud-Héraud¹, J. González-Nuevo^{68,86}, K. M. Górski^{69,101}, S. Gratton^{71,65}, A. Gregorio^{37,48}, A. Gruppuso⁴⁹, F. K. Hansen⁶⁶, D. Hanson^{80,69,8}, D. Harrison^{65,71}, S. Henrot-Versillé⁷², C. Hernández-Monteagudo^{12,79}, D. Herranz⁶⁸, S. R. Hildebrandt¹⁰, E. Hivon^{61,95}, S. Ho²⁶, M. Hobson⁶, W. A. Holmes⁶⁹, A. Hornstrup¹⁶, W. Hovest⁷⁹, K. M. Huffenberger¹⁰⁰, S. Illic⁶⁰, T. R. Jaffe^{97,9}, A. H. Jaffe⁵⁶, J. Jasche⁶¹, W. C. Jones²⁸, M. Juvela²⁷, E. Keihänen²⁷, R. Keskitalo^{22,13}, T. S. Kisner⁷⁸, J. Knoche⁷⁹, L. Knox³⁰, M. Kunz^{17,60,3}, H. Kurki-Suonio^{27,44}, G. Lagache⁶⁰, A. Lähteenmäki^{2,44}, J.-M. Lamarre⁷³, M. Langer⁶⁰, A. Lasenby^{6,71}, R. J. Laureijs⁴², C. R. Lawrence⁶⁹, J. P. Leahy⁷⁰, R. Leonardi⁴¹, J. Lesgourgues^{94,85}, M. Liguori³³, P. B. Lilje⁶⁶, M. Linden-Vørnle¹⁶, M. López-Caniego⁶⁸, P. M. Lubin³¹, J. F. Macías-Pérez⁷⁶, B. Maffei⁷⁰, D. Maino^{36,50}, N. Mandolcsi^{49,5,34}, A. Mangilli⁶¹, A. Marcos-Caballero⁶⁸, M. Maris⁴⁸, D. J. Marshall⁷⁴, P. G. Martin⁸, E. Martínez-González⁶⁸, S. Masi³⁵, S. Matarrese³³, F. Matthai⁷⁹, P. Mazzotta³⁸, P. R. Meinhold³¹, A. Melchiorri^{35,52}, L. Mendes⁴¹, A. Mennella^{36,50}, M. Migliaccio^{65,71}, S. Mitra^{55,69}, M.-A. Miville-Deschénes^{60,8}, A. Moneti⁶¹, L. Montier^{97,9}, G. Morgante⁴⁹, D. Mortlock⁵⁶, A. Moss⁸⁸, D. Munshi⁸⁷, P. Naselsky^{82,39}, F. Nati³⁵, P. Natoli^{34,4,49}, C. B. Netterfield²⁰, H. U. Nørgaard-Nielsen¹⁶, F. Noviello⁷⁰, D. Novikov⁵⁶, I. Novikov⁸², S. Osborne⁹², C. A. Oxborrow¹⁶, F. Paci⁸⁶, L. Pagano^{35,52}, F. Pajot⁶⁰, D. Paoletti^{49,51}, B. Partridge⁴³, F. Pasian⁴⁸, G. Patanchon¹, O. Perdereau⁷², L. Perotto⁷⁶, F. Perrotta⁸⁶, F. Piacentini³⁵, M. Piat¹, E. Pierpaoli²⁴, D. Pietrobon⁶⁹, S. Plaszczynski⁷², E. Pointecouteau^{97,9}, G. Polenta^{4,47}, N. Ponthieu^{60,54}, L. Popa⁶³, T. Poutanen^{44,27,2}, G. W. Pratt⁷⁴, G. Prézeau^{10,69}, S. Prunet^{61,95}, J.-L. Puget⁶⁰, J. P. Rachen^{21,79}, B. Racine¹, R. Rebolo^{67,14,40}, M. Reinecke⁷⁹, M. Remazeilles^{60,1}, C. Renault⁷⁶, A. Renzi⁸⁶, S. Ricciardi⁴⁹, T. Riller⁷⁹, I. Ristorcelli^{97,9}, G. Rocha^{69,10}, C. Rosset¹, G. Roudier^{1,73,69}, M. Rowan-Robinson⁵⁶, J. A. Rubiño-Martín^{67,40}, B. Rusholme⁵⁷, M. Sandri⁴⁹, D. Santos⁷⁶, G. Savini⁸⁴, B. M. Schaefer⁹⁶, F. Schiavon⁴⁹, D. Scott²³, M. D. Seiffert^{69,10}, E. P. S. Shellard¹¹, L. D. Spencer⁸⁷, J.-L. Starck⁷⁴, V. Stolyarov^{6,71,91}, R. Stompor¹, R. Sudiwala⁸⁷, R. Sunyaev^{79,89}, F. Sureau⁷⁴, D. Sutton^{65,71}, A.-S. Suur-Uiski^{27,44}, J.-F. Sygnet⁶¹, J. A. Tauber⁴², D. Tavagnacco^{48,37}, L. Terenzi⁴⁹, L. Toffolatti^{19,68}, M. Tomasi⁵⁰, M. Tristram⁷², M. Tucci^{17,72}, J. Tuovinen⁸¹, G. Umana⁴⁵, L. Valenziano⁴⁹, J. Valiviita^{44,27,66}, B. Van Tent⁷⁷, J. Varis⁸¹, M. Viel^{48,53}, P. Vielva^{68*}, F. Villa⁴⁹, N. Vittorio³⁸, L. A. Wade⁶⁹, B. D. Wandelt^{61,95,32}, M. White²⁹, J.-Q. Xia⁸⁶, D. Yvon¹⁵, A. Zaccari⁴⁸, and A. Zonca³¹

(Affiliations can be found after the references)

Received 2013; accepted 2013

ABSTRACT

Based on Cosmic Microwave Background (CMB) maps from the 2013 *Planck* Mission data release, this paper presents the detection of the Integrated Sachs-Wolfe (ISW) effect, i.e., the correlation between the CMB and large-scale evolving gravitational potentials. The significance of detection ranges from 2 to 4 σ , depending on which method is used. We investigate three separate approaches, which cover essentially all previous studies, as well as breaking new ground. (i) Through correlation of the CMB with the *Planck* reconstructed gravitational lensing potential (for the first time). This detection is made using the lensing-induced bispectrum between the low- ℓ and high- ℓ temperature anisotropies; the correlation between lensing and the ISW effect has a significance close to 2.5 σ . (ii) Through cross-correlation with tracers of large-scale structure, yielding around 3 σ significance, based on a combination of radio (NVSS) and optical (SDSS) data. (iii) Using aperture photometry on stacked CMB fields at the locations of known large-scale structures, which yields and confirms, over a broader spectral range, a 4 σ signal when using a previously explored catalogue, but shows strong discrepancies in amplitude and scale compared to expectations. More recent catalogues give more moderate results, ranging from negligible to 2.5 σ at most, but with a more consistent scale and amplitude, the latter being still slightly above what is expected from numerical simulations within ΛCMD. Where they can be compared, these measurements are compatible with previous work using data from *WMAP*, which had already mapped these scales to the limits of cosmic variance. *Planck*'s broader frequency coverage allows for better foreground cleaning, and confirms that the signal is achromatic, bolstering the case for ISW detection. As a final step we use tracers of large-scale structure to filter the CMB data, presenting maps of the ISW temperature perturbation. These results provide complementary and independent evidence for the existence of a dark energy component that governs the current accelerated expansion of the Universe.

Key words. Cosmology: observations – cosmic microwave background – large-scale structure of the Universe – dark energy – Galaxies: clusters: general – Methods: data analysis

* Corresponding author: P. Vielva vielva@ifca.unican.es

1. Introduction

This paper, one of a set associated with the 2013 data release from the *Planck*¹ mission (Planck Collaboration I 2013), presents the first results on the integrated Sachs-Wolfe (ISW) effect using *Planck* data. The ISW effect (Sachs & Wolfe 1967; Rees & Scrimgeour 1968; Hu & Sugiyama 1994) is a secondary anisotropy in the cosmic microwave background (CMB), caused by the interaction of CMB photons with the time-evolving potentials from large-scale structure (LSS, hereafter). Photons follow a geodesic that is weakly perturbed by the Newtonian gravitational potential, Φ , and experience a fractional shift in their temperature given by

$$\Theta = \frac{\Delta T}{T_{\text{CMB}}} = \frac{2}{c^3} \int_{\eta_*}^{\eta_0} d\eta \frac{\partial \Phi}{\partial \eta}, \quad (1)$$

where the integral is expressed in terms of the conformal time η , defined differentially by $d\eta/da = 1/(a^2 H(a))$ with $H(a)$ the Hubble function and a the scale factor. The integration limits here go from the recombination time (η_*) to the present time (η_0).

The sensitivity of the ISW effect to gravitational potentials (that can extend over Gpc scales) results in the power of the ISW being concentrated on the largest scales. The largest scales for the CMB have been mapped out by the *Wilkinson Microwave Anisotropy Probe* (*WMAP*) to the statistical limit of cosmic variance. Some systematics (like foreground removal) can have an impact on the reconstruction of the CMB especially at the largest scales where our Galaxy can introduce significant residuals on the reconstructed CMB map. The superior sensitivity of *Planck* together with its better angular resolution and wider frequency coverage allows for a better understanding (and hence removal) of Galactic and extragalactic foregrounds, therefore reducing the possible negative impact of these residuals. *Planck* allows us to improve on previous measurements by having a better systematic control, an improved removal of foregrounds (that permits us to explore the achromatic nature of the ISW signal on a wider frequency range), and a better understanding of systematics affecting tracer catalogues.

For cosmological models where $\Omega_m = 1$, gravitational potentials remain constant during linear structure formation, and the ISW signal is negligible (to first order, although second order nonlinear ISW is always expected around smaller over- and under-dense regions). In the presence of dark energy, decaying potentials due to the accelerated expansion rate, result in a net ISW effect which is positive when the CMB photons cross overdense regions and negative when the CMB photons cross underdense regions. Therefore, the ISW effect is an indicator of either non-zero curvature (Kamionkowski & Spergel 1994), any form of dark energy, such as a cosmological constant Λ (Crittenden & Turok 1996), modified gravity (Hu 2002), or a combination of these possibilities. By measuring the rate at which gravitational potentials in the LSS decay (up to redshift of around 2), the ISW effect can be used as an independent probe of cosmology and provides complementary and independent evidence for dark energy.

Detection of the ISW effect was first made possible with all-sky CMB maps from *WMAP*. Based on these data, many

works can be found in the literature where the authors aim at making, and subsequently improving, the measurement of the ISW effect through correlations with tracer catalogues: 2MASS (an infrared catalogue at low redshifts around 0.1, Afshordi et al. 2004; Dupé et al. 2011; Francis & Peacock 2009; Rassat et al. 2006), *HEAO* (an X-ray survey at low redshift, with the first positive claim for detection, Boughn & Crittenden 2004), Sloan Digital Sky Survey (SDSS, optical survey at intermediate redshifts, Bielby et al. 2010; Cabré et al. 2006; Fosalba et al. 2003; Fosalba & Gaztañaga 2004; Giannantonio et al. 2006; Granett et al. 2009; López-Corredoira et al. 2010; Padmanabhan et al. 2005; Sawangwit et al. 2010; Scranton et al. 2003; Xia 2009), the NRAO VLA Sky Survey (NVSS, radio catalogue with high-redshift sources, Boughn & Crittenden 2005; Hernández-Monteagudo 2010; Massardi et al. 2010; McEwen et al. 2007; Pietrobon et al. 2006a; Raccanelli et al. 2008; Schiavon et al. 2012; Vielva et al. 2006), and combined measurements with multiple tracers (Corasaniti et al. 2005; Gaztañaga et al. 2006; Giannantonio et al. 2008, 2012; Ho et al. 2008; Nolta et al. 2004). The significance of the ISW detections that can be found in the literature range between 0.9σ and 4.7σ . There are a number of peculiarities related to some of the detection claims, as noted by Hernández-Monteagudo (2010) and López-Corredoira et al. (2010). They both found lower significance levels than some previous studies and pointed out the absence of the signal at low multipoles where the ISW effect should be most prominent and the presence of point source emission on small scales for radio surveys.

The main result that is obtained from an ISW detection is a constraint on the cosmological constant (or dark energy), Ω_Λ . The general consensus from the variety of ISW analyses is for a value of $\Omega_\Lambda \simeq 0.75$ with an error of about 20%, which provides independent evidence for the existence of dark energy (Fosalba et al. 2003; Fosalba & Gaztañaga 2004; Nolta et al. 2004; Corasaniti et al. 2005; Padmanabhan et al. 2005; Cabré et al. 2006; Giannantonio et al. 2006; Pietrobon et al. 2006b; Rassat et al. 2006; Vielva et al. 2006; McEwen et al. 2007; Ho et al. 2008). All tests on spatial flatness find an upper limit for Ω_K of a few percent (Nolta et al. 2004; Gaztañaga et al. 2006; Ho et al. 2008; Li & Xia 2010). Using a prior on spatial flatness, the dark energy equation of state parameter, w , was found to be close to -1 (Giannantonio et al. 2006; Vielva et al. 2006; Ho et al. 2008) and has been excluded from having a strong time evolution (Giannantonio et al. 2008; Li & Xia 2010).

The ISW effect is achromatic, conserving the Planck spectrum of the CMB and can be separated from other CMB fluctuations through cross-correlations with catalogues which trace the LSS gravitational potentials (see for instance Crittenden & Turok 1996). This cross-correlation can be studied in different ways: angular cross-correlations in real space between the CMB and the catalogues tracing the LSS; the corresponding angular cross-power spectrum of the Fourier-transformed maps; or through the covariance of wavelet-filtered maps as a function of wavelet scale. The studies using *WMAP* data mentioned above follow this survey cross-correlation technique.

An alternative approach, similar to the angular cross-correlation in real space, consists of stacking CMB fields centred on known supersclusters or supervoids (Granett et al. 2008a,b; Pápai & Szapudi 2010). The advantage of this technique is that it allows for a detailed study of the profile of the CMB fluctuations caused by this secondary anisotropy.

A novel and powerful approach takes advantage of the fact that the same potentials that make CMB photons gain or lose energy along their path (ISW), create lensing distortions that can

¹ *Planck* (<http://www.esa.int/Planck>) is a project of the European Space Agency (ESA) with instruments provided by two scientific consortia funded by ESA member states (in particular the lead countries France and Italy), with contributions from NASA (USA) and telescope reflectors provided by a collaboration between ESA and a scientific consortium led and funded by Denmark.

be measured from the CMB map directly (e.g., [Hu & Okamoto 2002](#)). The interplay between weak gravitational lensing and the ISW effect causes a non-Gaussian contribution to the CMB, which can be measured through the lensing-induced bispectrum between small and large angular scales. The measurement of the lensing potential requires a large number of modes that could not be measured before the arrival of *Planck* data.

This paper presents new measurements of the ISW effect carried out with *Planck*. Even although our detections are not in every case as strong as some previously claimed significance levels, we believe that our results are an improvement over earlier studies. This is because we can use the additional power enabled by the frequency coverage and sensitivity of *Planck*. To establish this we carry out a comprehensive study of all the main approaches which have previously been taken to estimate the ISW signal. We also present new results in relation to the non-Gaussian structure induced by the ISW effect.

The paper is organized as follows: In Sect. 2 we describe the data used in this work (both for the CMB and large-scale structure). The first ever results on the estimation of the lensing-induced bispectrum are presented in Sect. 3. Cross-correlations with external surveys are investigated in Sect. 4, and in Sect. 5 we present the results for the stacking analysis on the temperature maps, as well as aperture photometry on super-clusters and super-voids. The recovery of the ISW all-sky map is described in Sect. 6. Finally, we discuss our main results and their cosmological implications in Sect. 7.

2. Data description

In this Section we describe the different data sets used in this paper. This includes *Planck* data (the CMB temperature and lensing potential maps, see [Planck Collaboration I 2013](#); [Planck Collaboration XII 2013](#); [Planck Collaboration XVII 2013](#)) we refer to the corresponding *Planck* papers for details) and external data sets (large-scale structure tracers) used in the ISW determination: the radio NVSS catalogue; optical Luminous Galaxies (CMASS/LOWZ) and the Main Galaxy Sample from the Sloan Digital Sky Survey (SDSS); as well as several superstructure catalogues.

2.1. Planck data

Planck data and products used in this paper are described in the following sections, in particular the foreground-cleaned CMB maps produced by the *Planck* component separation pipelines, and related products, such as dedicated component-separated frequency maps ([Planck Collaboration XII 2013](#)), as well as the *Planck* lensing map ([Planck Collaboration XVII 2013](#)).

2.1.1. CMB maps

For the present work we have made use of the *Planck* foreground-cleaned CMB maps provided by the data processing centres (as described in the *Planck* component separation paper [Planck Collaboration XII 2013](#)). In particular, to test robustness, some of the results are presented for different cleaned CMB maps, which were constructed using four different component separation techniques: **Commdore-Ruler** (C-R, which uses physical parametrization); NILC (an internal linear combination technique); SEVEM (a template fitting method); and SMICA (which uses spectral matching). Since the contribution of the ISW signal is only important on large scales, low resolution

maps, with HEALPix [Górski et al. \(2005\)](#) parameter $N_{\text{side}} = 64$, and pixel size of about 55 arcmin, have been used for most of the analyses. One exception is the study of the correlation between the ISW and lensing signals, which requires the use of full-resolution maps ($N_{\text{side}}=2048$, pixel size of 1.7 arcmin). The maps are degraded directly from the original full resolution down to the corresponding N_{side} .

In addition, foreground-cleaned maps per frequency (from 44 to 353 GHz) at resolution $N_{\text{side}} = 512$ were used for the stacking analysis presented in Sect. 5. These maps were constructed by subtracting a linear combination of internal templates using SEVEM (see the SEVEM Appendix of [Planck Collaboration XII 2013](#), for a detailed description of the method). As an example the SEVEM CMB map is shown in Fig. 1 (left panel).

Finally, to minimize the presence of foreground contamination in the maps, we have used the official mask described in [Planck Collaboration XII \(2013\)](#), which excludes regions with larger Galactic and point-source contamination (the U73 mask). This mask is given at the full *Planck* resolution and is downgraded to the required levels. The downgrading procedure consists of the following steps: the mask (originally a map with zero and one values) is convolved with a Gaussian beam of FWHM three times the characteristic pixel size of the final N_{side} resolution; this convolved map is then degraded to the required N_{side} , and, afterwards, a threshold of 0.75 is imposed (i.e., pixels with a value above this threshold are set to one, whereas the rest are set to zero).

2.1.2. Lensing potential map

Weak gravitational lensing distorts the CMB temperature anisotropy pattern. This effect is sensitive to the projected matter distribution in the large-scale structure at high redshifts, where structure growth is linear and the statistics close to Gaussian. Weak lensing causes correlations between different multipoles which are proportional to the lensing deflection field. These correlations can be exploited for reconstructing the density field and for measuring its statistical properties ([Hu & Okamoto 2002](#); [Okamoto & Hu 2003](#)). The lensing effect in the CMB can be estimated by this homogeneity breaking, and in this way individual modes of the lensing potential at multipoles $\ell < 100$ can be reconstructed with a significance of around 0.5σ , showing the necessity of a statistical treatment. Nevertheless the overall effect of the lensing is measured to better than 25σ ([Planck Collaboration XVII 2013](#)). The additional lensing effect in the temperature power spectrum is detectable with a significance of about 10σ ([Planck Collaboration XV 2013](#)).

With *Planck* data, we aim at detecting a correlation between the ISW effect and the lensing potential, where the latter is a tracer of the large-scale structure at high redshift. This correlation is restricted to 9σ , even in the ideal case, limited by cosmic variance and the smallness of the ISW effect in comparison to the primary CMB ([Lewis et al. 2011](#)). The data products used in this study are the *Planck* lensing potential reconstruction, and specific lensing maps obtained from the component separation pipelines. The lensing potential is available as part of the first *Planck* data release. Its detailed development is described in the *Planck* lensing paper ([Planck Collaboration XVII 2013](#)). In Fig. 1 we reproduce (right panel) an optimally filtered version of the *Planck* lensing map, suitable for the ISW-lensing cross-correlation.

In addition to a direct correlation between the CMB sky and the reconstructed lensing map, we measure the bispectrum generated by weak lensing by applying a range of estimators: the

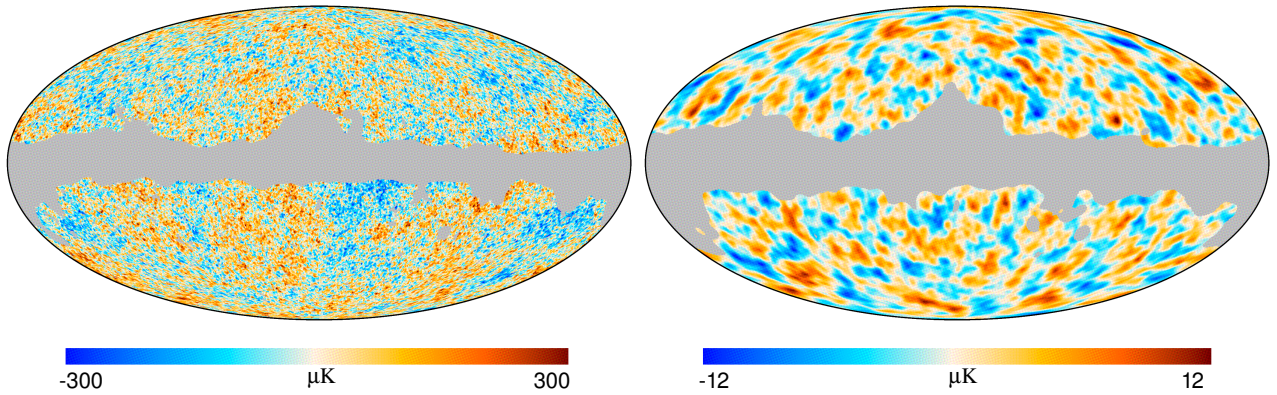


Fig. 1. *Left:* one of the CMB used in this paper, constructed using SEVEM (given at $N_{\text{side}} = 64$). Other *Planck* CMB maps used in this work are Commander-Ruler, NILC and SMICA, in addition to clean SEVEM maps from 44 to 353 GHz. *Right:* *Planck* lensing map, optimally filtered to perform the ISW-lensing cross-correlation (given at $N_{\text{side}} = 1024$).

KSW-bispectrum estimator; bispectra binned in multipole intervals; and a modal decomposition of the bispectrum. This measurement is made possible for the first time thanks to the *Planck* data. In addition, we will use information from the lensing field as a tracer for an ISW map reconstruction at high redshift (see Sect. 6).

2.2. External data sets

As described in the introduction, the achromatic nature of the ISW effect requires a tracer of the gravitational potentials from the large-scale structure, so that by cross-correlating the CMB temperature map with that tracer distribution the fluctuations due to the ISW effect are singled out. The prerequisites for a tracer catalogue to be used in ISW studies are: a large survey volume; well-understood biasing properties; and low or at least well-modelled systematics. The radio NVSS catalogue and the optical Luminous Galaxies (SDSS-CMASS/LOWZ) and Main Galaxy Sample (SDSS-MG) catalogues possess these qualities. Table 7 summarizes some basic properties of these catalogues. In addition, the redshift distributions of these catalogues are shown in Fig. 2. Notice that NVSS presents the widest redshift coverage. The SDSS-CMASS/LOWZ sample is peaked around $z \approx 0.5$, whereas the SDSS-MG sample peaks around $z \approx 0.3$.

Figure 3 shows the all-sky density projection for these maps, where the grey area indicates regions not observed by these surveys (or discarded for having contamination or low galaxy number density, see next subsections for details). In Fig. 4 we give the angular power spectra (blue points) of the surveys (corrected with a procedure similar to MASTER, e.g., Hivon et al. 2002), as well as the theoretical spectra (black lines) and their 1σ error bars (grey areas), estimated from the MASTER approach as well.

Besides the cross-correlation between CMB and LSS tracers (Sect. 4), we will present results from a different methodology in Sect. 5, where we use catalogues of super-structures to study the ISW through stacking of the CMB fluctuations on the positions of these super-structures. The relevant catalogues are described in Sect. 2.2.4.

2.2.1. NVSS radio catalogues

Luminous Active Galactic Nuclei (hereafter AGN) are known to be powerful radio sources, visible out to high redshifts. These

Table 1. Major characteristics of the galaxy catalogues used as tracers of the gravitational potential. From left to right, the columns indicate: the number of galaxies per steradian; the fraction of the sky covered by each survey; the mean bias; and the median redshift. Notice that the bias for NVSS is not provided, since the assumed model has a bias which depends on redshift (see text for details).

Galaxy catalogue	\bar{n}	f_{sky}	bias	\bar{z}
NVSS	1.584×10^5	0.73		1.17
SDSS-CMASS/LOWZ	5.558×10^5	0.22	2.03	0.45
SDSS-MG	9.680×10^6	0.22	1.20	0.32

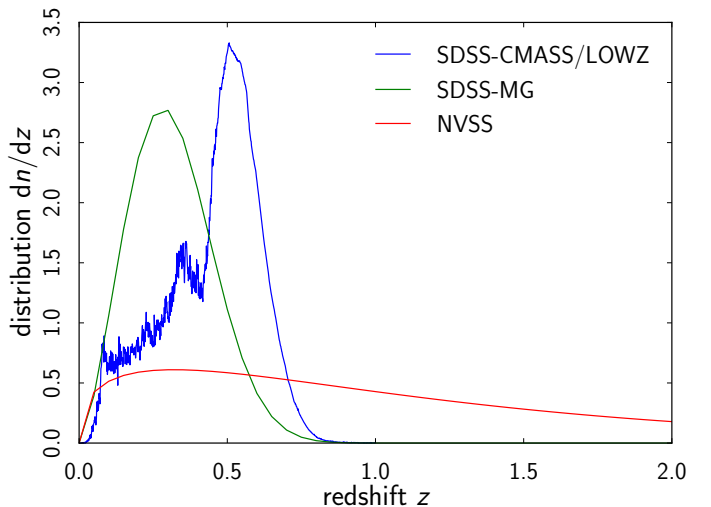


Fig. 2. Redshift distributions of the different surveys used in this work as LSS tracers, to be correlated with the *Planck* CMB maps. For ease of comparison, these distributions have been normalised to unity.

sources are hence able to probe the cosmic density field during the entire redshift range from matter domination to accelerated expansion due to dark energy. If AGN are fair tracers of the underlying density field, these sources should likewise probe the spatial distribution of the large-scale potential wells that decay

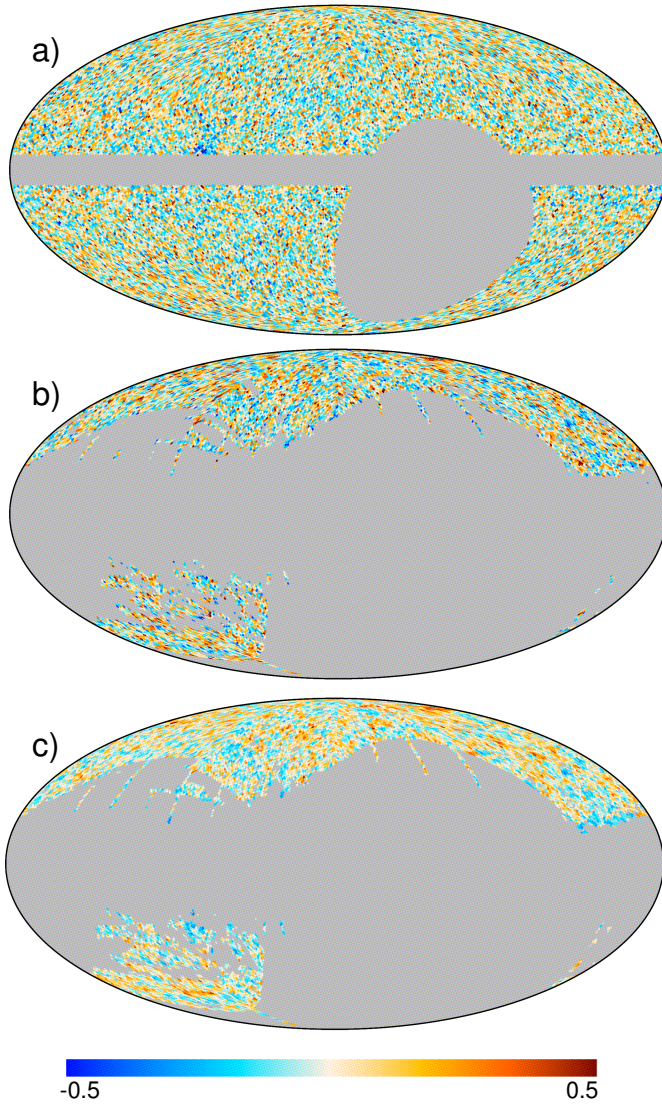


Fig. 3. Density contrast maps obtained from the galaxy catalogues at $N_{\text{side}} = 64$. From top to bottom: NVSS; SDSS-CMASS/LOWZ; and SDSS-MG.

at late times after the accelerated expansion sets in and generates the ISW effect.

We shall focus on a single radio survey, with the level of sensitivity and sky coverage required for ISW studies, namely the NRAO VLA Sky Survey (hereafter NVSS, Condon et al. 1998). This survey was conducted using the Very Large Array (VLA) at 1.4 GHz, and covers up to an equatorial latitude of $b_E = -40^\circ$, with an average noise level of $0.45 \text{ mJy beam}^{-1}$. It results in roughly 1.4×10^6 sources above a flux threshold of 2.5 mJy. Fig. 3 displays the number density map computed from the NVSS survey (top panel). The AGN population is known to be dominant in radio catalogues at 1.4 GHz in the high flux density regime. Condon et al. (1998) show that at this frequency, star-forming galaxies (SFGs) contribute about 30% of the total number of weighted source counts above 1 mJy, but their presence decreases rapidly as higher flux thresholds are adopted. The NVSS SFGs are nearby sources ($z < 0.01$), and hence may distort the ability of our radio template to probe the intermediate and high redshift density field.

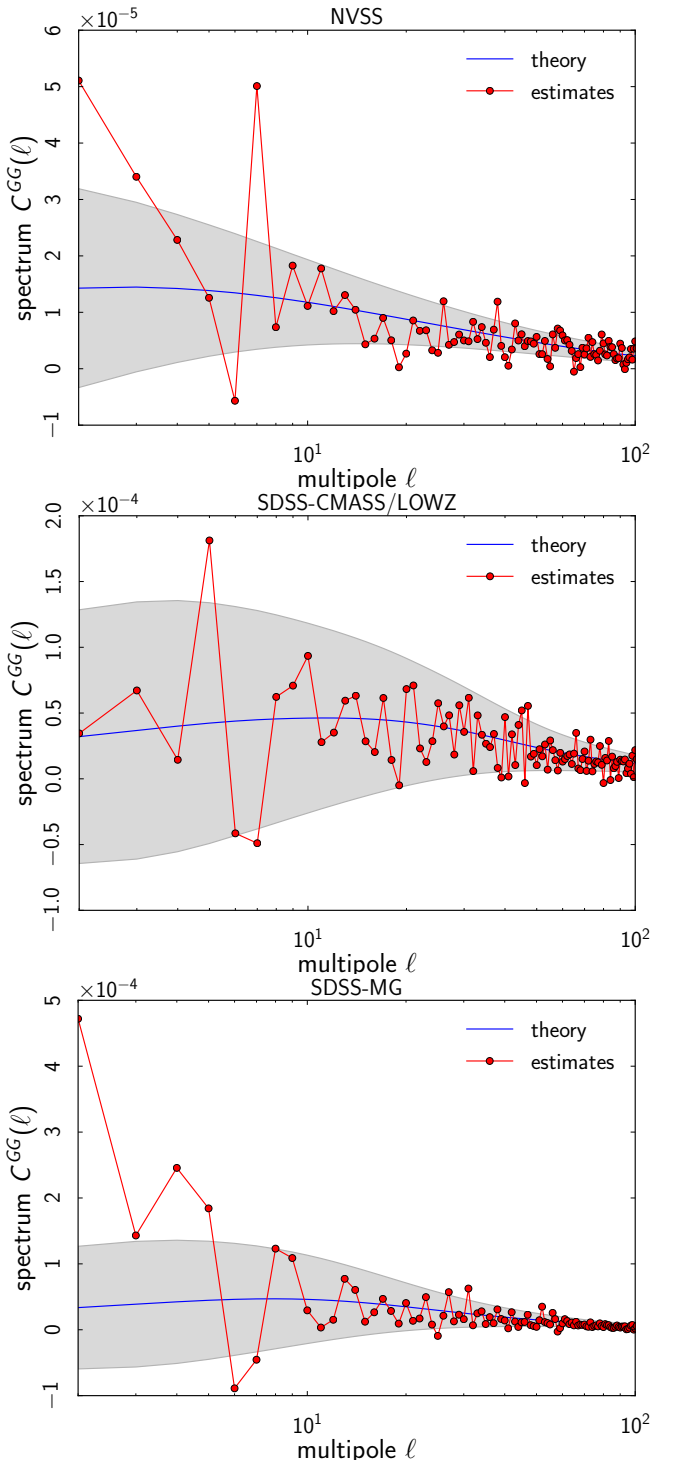


Fig. 4. Angular power spectra from the maps in Fig. 3. From top to bottom: NVSS; SDSS-CMASS/LOWZ; and SDSS-MG. The observed spectra are the red points, whereas the theoretical models are represented by the black lines (the grey areas correspond to the sampling variance).

We next address the presence of systematic effects in the NVSS survey. Two different antenna configurations were used while conducting the NVSS survey: the D-configuration (for $b_E \in [-10^\circ, 78^\circ]$), and the DnC-configuration for large zenith angles ($b_E < -10^\circ$, $b_E > 78^\circ$). This change in the antenna configuration is known to introduce changes in the source number density above 2.5 mJy, as first pointed out by Blake & Wall

(2002). The NVSS map at 2.5 mJy is corrected for this declination systematic using the following procedure: the sky is divided into equatorial strips and the mean number of sources in each strip is re-normalised to the full sky mean (see e.g., Vielva et al. 2006). With this procedure the average number of sources in the NVSS map is the same as before the correction, and hence the shot noise level does not change. The number of strips into which the map is divided is 70, but the results are independent of this choice.

Regarding the galaxy bias, in this work we adopt the Gaussian bias evolution model of Xia et al. (2011). If $n(M, z)$ is the halo mass function and $b(M, z)$ is the bias of halos with comoving mass M , then the bias of the survey is given by a mass-weighted integral,

$$b(z) = \frac{\int_{M_{\min}}^{\infty} dM b(M, z) M n(M, z)}{\int_{M_{\min}}^{\infty} dM M n(M, z)}. \quad (2)$$

This model depends on the minimum mass M_{\min} of halos present in the survey. The upper limit in the mass is taken to be infinity because the effect of the high mass end on the bias is negligible. Marcos-Caballero et al. (2013) proposed a theoretical model for the NVSS angular power spectrum, which also takes into account the information of the redshift distribution given by CENSORS data (Brookes et al. 2008). The redshift distribution is parametrized by

$$\frac{dn}{dz} = n_0 \left(\frac{z}{z_0} \right)^{\alpha} e^{-az/z_0}, \quad (3)$$

where $z_0 = 0.32$ and $\alpha = 0.36$. The parameter n_0 is a constant in order to have a distribution normalized to unity. This function is represented in Fig. 2. The bias follows the prescription of Eq. 2, with M_{\min} equal to $10^{12.67} M_{\odot}$, where the Sheth-Tormen (Sheth & Tormen 1999) mass function is adopted. Hereafter this model will be regarded as our fiducial model for NVSS.

2.2.2. SDSS Luminous Galaxies

For this analysis we use the photometric Luminous Galaxy (LG) catalogue from the Baryonic Oscillation Spectroscopic Survey (BOSS) of the SDSS III. The data used consist of two subsamples: CMASS; and LOWZ. Both samples are combined to form a unique LG map (see Fig. 3, second panel). Hereafter, these samples will be referred to as SDSS-CMASS, SDSS-LOWZ, and SDSS-CMASS/LOWZ, for the combination.

SDSS-CMASS

We use the BOSS targets chosen to have roughly constant stellar mass and known as the photometric ‘‘CMASS’’ sample. This sample is mostly contained in the redshift range $z = 0.4\text{--}0.7$, with a galaxy number density close to 110 deg^{-2} , and is selected after applying the colour cuts explained in Ross et al. (2011).

While such color selection yields a catalogue of about 1,600,000 galaxies, further cuts needed to be applied in order to account for dust extinction (based on the maps by Schlegel et al. 1998 with the criterion $E(B - V) < 0.08$), for seeing in the r band (required to be $< 2.0''$) and for the presence of bright stars, similar to Ho et al. (2012). Finally, we neglected all pixels with a mask value inferred from the footprint below 0.9 on a HEALPix map of resolution $N_{\text{side}}=64$. This procedure left about one million sources $10,500 \text{ deg}^2$. Photometric redshifts of this sample are calibrated using a selection of about 100,000 BOSS spectra

as a training sample for the photometric catalogue. These LGs are among the most luminous galaxies in the Universe and therefore allow for a good sampling of the largest scales. Given the large number of such sources included in the sample, shot-noise does not dominate clustering errors. According to Ross et al. (2011), about 3.7 % of these objects are either stars or quasars, and this makes further corrections necessary, as explained at the end of this section.

SDSS-LOWZ

The photometric LOWZ sample is one of the two galaxy samples targeted by the BOSS of Sloan III. It selectd luminous, highly biased, mostly red galaxies, placed at an average redshift of $\langle z \rangle \sim 0.3$ and below the redshifts of the CMASS sample ($z < 0.4$). Our selection criteria in terms of the Sloan five model magnitudes $ugriz$ follow those given in Sect. 2 of Parejko et al. (2013). With a total number of sources close to 600,000, this photometric sample contains a higher number density of galaxies in the southern part of the footprint than in the northern one (by more than 3 %), which seems to be at odds with Λ CDM predictions. However, most of this effect vanishes when we subtract the dipole in the effective area under analysis, in such a way that the low ℓ range of the auto power spectrum is consistent with a Λ CDM model and a constant bias $b \simeq 2$ (Hernandez-Monteagudo et al. 2013).

Both SDSS-CMASS and SDSS-LOWZ samples are further corrected for any scaling introduced by possible systematics like stars, mask value, seeing, sky emission, airmass and dust extinction. Following exactly the same procedure as in Hernandez-Monteagudo et al. (2013), we find that both LG samples are contaminated by stars, in the sense that the galaxy number density decreases in areas with higher star density, since the latter tend to ‘‘blind’’ galaxy detection algorithms.

2.2.3. Main SDSS Galaxy Sample

We use a sample of photometrically-selected galaxies from the SDSS-DR8 catalogue, which covers a total sky area of $14,555 \text{ deg}^2$ (Aihara et al. 2011). The total number of objects labelled as galaxies in this data release is 208 million. From this catalogue, and following Cabré et al. (2006), we define a sub-sample by selecting only objects within the range $18 < r < 21$, where this r -band model magnitude corrected for extinction. Following Giannantonio et al. (2008), we also restrict our sub-sample to objects with redshifts $0.1 < z < 0.9$, and with measured redshift errors such that $\sigma_z < 0.5z$. We rely on the photometric redshift estimates of the SDSS photo- z primary galaxy table, which have been obtained through a ‘‘kd-tree’’ nearest neighbour technique, by fitting the spectroscopic objects observed with similar colour and inclination angle. The total number of galaxies in our final sample is about 42 million, with redshifts distributed around a median value of around 0.35, as shown in Fig. 2. To avoid possible errors introduced by singularities in the photometric redshifts estimates, instead of using the real observed redshift distribution in our analysis we resort to the analytical function

$$\frac{dn}{dz} = \frac{\beta}{\Gamma(\frac{m+1}{\beta})} \frac{z^m}{z_0^{m+1}} e^{-(z/z_0)^{\beta}}, \quad (4)$$

which is fitted to the data, with parameters $m = 1.5$, $\beta = 2.3$ and $z_0 = 0.34$, which are identical to those found by Giannantonio et al. (2012). For the galactic bias we use the value $b = 1.2$,

which is found by Giannantonio et al. (2012) by fitting the Λ CDM prediction to the observed auto-correlation function of the galaxies, and we adopt their proposed mask.

2.2.4. SDSS, super-structures

Granett et al. (2008b) produced a sample² of 50 superclusters and 50 supervoids identified from the Luminous Red Galaxies (LRGs) in the SDSS (sixth data release, DR6, Adelman-McCarthy et al. 2008) that covers an area of 7500 deg^2 on the sky. They used publicly available algorithms, based on the Voronoi tessellation, to find 2836 superclusters (using VOBOZ, VOronoi BOund Zones, Neyrinck et al. 2005) and 631 supervoids (using ZOBOV, ZOnes Bordering On Voidness, Neyrinck 2008) above a 2σ significance level (defined as the probability of obtaining, in a uniform Poisson point sample, the same density contrasts as those of clusters and voids). The 50 superclusters and 50 supervoids they published in their catalogue correspond to density contrasts of about 3σ and 3.3σ respectively. They span a redshift range of $0.4 < z < 0.75$, with a median of around 0.5, and inhabit a volume of about $5 h^{-3} \text{ Gpc}^3$. These superstructures can potentially produce measurable ISW signals, as suggested in Granett et al. (2008a,b). For each structure, the catalogue provides: the position on the sky of the centre; the mean and maximum angular distance between the galaxies in the structure and its centre; the physical volume; and three different measures of the density contrast (calculated from all its Voronoi cells, from only its over- or under-dense cells, and from only its most over- under-dense cell). For the present paper, we concentrate on using the supervoid catalogue by Granett et al. (2008b), as they can be compared with two other, more recent catalogues of voids.

The second catalogue of cosmic voids that we consider here is published by Pan et al. (2012)³. It has been built from the seventh data release (DR7) of the SDSS. Using the VoidFinder algorithm (Hoyle & Vogeley 2002), they identified 1055 voids with redshifts smaller than $z = 0.1$. Each void is listed with its position on the sky, its physical radius (defined as the radius of the maximal sphere enclosing the void), an effective radius defined as the radius of a sphere of the same volume, its physical distance to us, its volume and mean density contrast. The filling factor of the voids in the sample volume is 62 %. The largest void is just over 47 Mpc in effective radius, while the median effective radius of the void sample is roughly 25 Mpc. Some of the voids are both very close to us and relatively large (larger than 30 Mpc in radius), which results in large angular sizes of up to 15° .

The third void catalogue that we use has been released by Sutter et al. (2012) and also made publicly available.⁴ Note that it is being updated regularly, and the results reported here are based on the 21 February 2013 version of the catalogue. Using their own improved version of ZOBOV, these authors identified 1495 voids distributed across the 0–0.44 redshift range. They subdivided their catalogue into six subsamples: *dim1*, *dim2*, *bright1* and *bright2*, constructed from the main SDSS; and *lrgdim*, *lrbright* built from the SDSS LRG sample. For each void, the information provided includes the position of the centre, the redshift, the volume, the effective radius, and the density contrast.

² Available at <http://ifa.hawaii.edu/cosmowave/supervoids/>.

³ Available at <http://www.physics.drexel.edu/~pan/>.

⁴ Available at <http://www.cosmicvoids.net>.

3. ISW-lensing bispectrum

There is an interesting interplay between gravitational lensing of the CMB and the ISW effect, which manifests itself as a non-Gaussian feature. CMB-lensing can be described by a convolution of the CMB-temperature map T with the weak lensing potential ϕ ,

$$T(\ell) \rightarrow T(\ell) - \int \frac{d^2\ell'}{2\pi} \ell'(\ell - \ell') \phi(\ell - \ell') T(\ell'). \quad (5)$$

The CMB lensing can be measured by a direct estimate of the CMB bispectrum, because the bispectrum acquires first order terms proportional to the product of two power spectra $\tilde{C}_\ell^{\text{TT}} C_\ell^{\text{T}\phi}$, where $\tilde{C}_\ell^{\text{TT}}$ is the lensed temperature power spectrum and $C_\ell^{\text{T}\phi}$ is the temperature-potential cross-power spectrum. The potential field ϕ and the temperature field T are correlated, because ϕ , which deflects the CMB photons, also gives rise to the ISW effect in T (Hu & Okamoto 2002; Seljak & Zaldarriaga 1999; Verde & Spergel 2002; Giovi et al. 2003). This secondary bispectrum contains new information about the cosmological redshift, because it is generated mainly at redshifts larger than unity, and biases measurements of the primordial bispectrum. The term $C_\ell^{\text{T}\phi}$ correlates the CMB temperature on small scales with the lensing potential on large scales, and causes the bispectrum to assume large amplitudes in the squeezed triangles configuration (see e.g., Goldberg & Spergel 1999; Seljak & Zaldarriaga 1999; Hu 2000; Giovi et al. 2003; Okamoto & Hu 2003; Giovi & Baccigalupi 2005; Lewis & Challinor 2006; Serra & Cooray 2008; Mangilli & Verde 2009; Hanson et al. 2009, 2010; Smith & Zaldarriaga 2011; Lewis et al. 2011).

Due to the rotational invariance of the sky, the CMB angular bispectrum $\langle a_{\ell_1 m_1} a_{\ell_2 m_2} a_{\ell_3 m_3} \rangle$ can be factorized as follows:

$$\langle a_{\ell_1 m_1} a_{\ell_2 m_2} a_{\ell_3 m_3} \rangle = \mathcal{G}_{\ell_1 \ell_2 \ell_3}^{m_1 m_2 m_3} b_{\ell_1 \ell_2 \ell_3}, \quad (6)$$

where $\mathcal{G}_{\ell_1 \ell_2 \ell_3}^{m_1 m_2 m_3} \equiv \int d\Omega Y_{\ell_1}^{m_1}(\hat{n}) Y_{\ell_2}^{m_2}(\hat{n}) Y_{\ell_3}^{m_3}(\hat{n})$ is the Gaunt-integral and $b_{\ell_1 \ell_2 \ell_3}$ is the so-called reduced bispectrum. In the case where the bispectral signal on the sky is due to the ISW-lensing effect, $b_{\ell_1 \ell_2 \ell_3} = A^{\text{T}\phi} b_{\ell_1 \ell_2 \ell_3}^{\text{lens-ISW}}$, where $A^{\text{T}\phi}$ parametrizes the amplitude of the effect and

$$b_{\ell_1 \ell_2 \ell_3}^{\text{lens-ISW}} = \left\{ \frac{\ell_1(\ell_1 + 1) - \ell_2(\ell_2 + 1) + \ell_3(\ell_3 + 1)}{2} C_{\ell_1}^{\text{T}\phi} \tilde{C}_{\ell_3}^{\text{TT}} \right. \\ \left. + (5 \text{ permutations}) \right\}. \quad (7)$$

A more general expression for intensity and polarization can be found in Lewis et al. (2011). Estimation of the bispectrum then yields a measurement of $A^{\text{T}\phi}$.

We can also define an alternative rotationally-invariant reduced bispectrum $B_{\ell_1 \ell_2 \ell_3}$ as $B_{\ell_1 \ell_2 \ell_3} = h_{\ell_1 \ell_2 \ell_3}^2 b_{\ell_1 \ell_2 \ell_3}$, where

$$h_{\ell_1 \ell_2 \ell_3}^2 \equiv \sum_{m_1 m_2 m_3} (\mathcal{G}_{\ell_1 \ell_2 \ell_3}^{m_1 m_2 m_3})^2 \\ = \frac{(2\ell_1 + 1)(2\ell_2 + 1)(2\ell_3 + 1)}{4\pi} \begin{pmatrix} \ell_1 & \ell_2 & \ell_3 \\ 0 & 0 & 0 \end{pmatrix}^2. \quad (8)$$

The interest in $B_{\ell_1 \ell_2 \ell_3}$ is that it can be directly estimated from the observed map using the expression

$$B_{\ell_1 \ell_2 \ell_3}^{\text{obs}} = \int d\Omega T_{\ell_1}(\Omega) T_{\ell_2}(\Omega) T_{\ell_3}(\Omega), \quad (9)$$

where the filtered maps $T_\ell(\Omega)$ are defined as

$$T_\ell(\Omega) \equiv \sum_m a_{\ell m} Y_{\ell m}(\Omega). \quad (10)$$

By basically combining the single- ℓ estimates $B^{\text{obs}}/B^{\text{lens-ISW}}$ for $A^{\text{T}\phi}$ using inverse variance weighting, the ISW-lensing bispectrum estimator can be written as (see Planck Collaboration XXIV 2013, for more details)

$$\hat{A}^{\text{T}\phi} = \frac{\langle B^{\text{lens-ISW}}, (B^{\text{obs}} - B^{\text{lin}}) \rangle}{\langle B^{\text{lens-ISW}}, B^{\text{lens-ISW}} \rangle}, \quad (11)$$

where the inner product is defined by

$$\langle B^i, B^j \rangle \equiv \sum_{\ell_1 \leq \ell_2 \leq \ell_3} \frac{B^i_{\ell_1 \ell_2 \ell_3} B^j_{\ell_1 \ell_2 \ell_3}}{V_{\ell_1 \ell_2 \ell_3}}. \quad (12)$$

Here, B^{lin} is a linear correction that has zero average but reduces the variance of the estimator in the presence of anisotropic noise and a mask. Furthermore, $V_{\ell_1 \ell_2 \ell_3} = g_{\ell_1 \ell_2 \ell_3} h_{\ell_1 \ell_2 \ell_3}^2 C_{\ell_1} C_{\ell_2} C_{\ell_3}$, with g being a simple permutation factor ($g = 6$ when all ℓ are equal, $g = 2$ when two ℓ are equal and $g = 1$ otherwise). As in all expressions in this section, we have implicitly taken the beam and noise of the experiment into account, e.g., C_ℓ should actually be $b_\ell^2 C_\ell + N_\ell$ with b_ℓ the beam transfer function and N_ℓ the noise power spectrum.

In Eq. 11 we have also used the fact that, as discussed in detail in Planck Collaboration XXIV (2013), the full inverse covariance weighting can be replaced by a diagonal covariance term, $(C^{-1}a)_{\ell m} \rightarrow a_{\ell m}/C_\ell$, without loss of optimality, if the masked regions of the map are filled in with a simple diffusive inpainting scheme.

The normalization of the lensing-ISW estimator in the denominator of Eq. 11 can be replaced by (see e.g. Lewis et al. 2011)

$$F = \sum_\ell \left(F_\ell^{-1} + \frac{1 + r_\ell^{-2}}{2\ell + 1} \right)^{-1}, \quad (13)$$

where $r_\ell \equiv C_\ell^{\text{T}\phi} / \sqrt{\tilde{C}_\ell^{\text{TT}} C_\ell^{\phi\phi}}$ parameterizes the deviation from the Cauchy-Schwarz relation and F_ℓ is given in terms of the ISW-lensing bispectrum (see for example Lewis et al. 2011). The first term in Eq. 13 corresponds to the Fisher errors assuming Gaussian $a_{\ell m}$. However, contrary to the null hypothesis that is assumed, for example, in the primordial bispectra (Gaussianity), there is an actual non-Gaussian signal already present in the ISW-lensing bispectrum. This guarantees a larger variance for the estimators than are included in the additional terms present in the previous equations.

An important issue is the impact of the ISW-lensing bispectrum on estimates of the primordial non-Gaussianity. Assuming weak levels of non-Gaussianity and considering both the primordial bispectrum $B_{\ell_1 \ell_2 \ell_3}^{\text{prim}}$ and the ISW-lensing bispectrum $B_{\ell_1 \ell_2 \ell_3}^{\text{lens-ISW}}$, one can compute the expected bias Δ induced in the primordial bispectrum using the formula:

$$\Delta^{\text{prim}} = \frac{\langle B^{\text{lens-ISW}}, B^{\text{prim}} \rangle}{\langle B^{\text{prim}}, B^{\text{prim}} \rangle} \quad (14)$$

with the inner product defined in Eq. 12. Predictions of this bias on the primordial f_{NL} for *Planck* resolution can be seen for example in Hanson et al. (2009), Mangilli & Verde (2009), Smith

& Zaldarriaga (2011), and Lewis et al. (2011). The most important bias is introduced to the local shape and, considering $\ell_{\text{max}} \sim 2000$, is expected to be $\Delta^{\text{local}} \sim 7$ (Planck Collaboration XXIV 2013).

3.1. ISW-lensing estimators

There are several implementations of the optimal estimator given in Eq. 11. For their detailed description in the context of *Planck* see Planck Collaboration XXIV (2013); Planck Collaboration XVII (2013). We have applied four of these implementations to *Planck* data in order to constrain the ISW-lensing bispectrum. Three of them represent a direct bispectrum estimation: the KSW estimator (Komatsu et al. 2005; Creminelli et al. 2006), the binned bispectrum (Bucher et al. 2010), and the modal decomposition (Fergusson et al. 2010). The remaining approach is based on a previous estimation of the gravitational lensing potential field Lewis et al. (2011). These estimators differ in the implementation and approximations that are used in order to compute the expression given in Eq. 11, the direct computation of which is out of reach of current computing facilities. They will be reviewed in the next subsections.

3.1.1. Lensing potential reconstruction

The estimator given in Eq. 6 can be written in terms of the lensing potential amplitude reconstruction $\hat{\phi}$ as

$$\hat{A}^{\text{T}\phi} \equiv \hat{S} = \frac{1}{N} \sum_{\ell m} C_\ell^{\text{T}\phi} \frac{\tilde{T}_{\ell m}}{\tilde{C}_\ell^{\text{TT}}} \frac{\hat{\phi}_{\ell m}^*}{N_\ell^{\phi\phi}}, \quad (15)$$

where $\hat{\phi}_{\ell m}^*$ can be estimated using a quadratic estimator (Okamoto & Hu 2003) and $N_\ell^{(0)}$ is given in terms of the ISW-lensing bispectrum (Lewis et al. 2011). Therefore, this estimator quantifies the amount of cross-correlation between the temperature map and the reconstruction of the lensing signal, and most of the correlation is found at multipoles below 100.

3.1.2. KSW-estimator

The KSW bispectrum estimator (Komatsu et al. 2005) for the ISW-lensing signal can be written as

$$\hat{A}^{\text{T}\phi} = (F^{-1}) \hat{S}, \quad (16)$$

where \hat{S} can be computed from data as

$$\begin{aligned} \hat{S} \equiv & \frac{1}{6} \sum_{\ell_1 m_1} \sum_{\ell_2 m_2} \sum_{\ell_3 m_3} \mathcal{G}_{\ell_1 \ell_2 \ell_3}^{m_1 m_2 m_3} b_{\ell_1 \ell_2 \ell_3}^{\text{lens-ISW}} \times \\ & [(C^{-1}a)_{\ell_1 m_1} (C^{-1}a)_{\ell_2 m_2} (C^{-1}a)_{\ell_3 m_3} - \\ & 3(C^{-1})_{\ell_1 m_1, \ell_2 m_2} (C^{-1}a)_{\ell_3 m_3}], \end{aligned} \quad (17)$$

and (F^{-1}) is the inverse of the ISW-lensing Fisher matrix F of Eq. 13. Details on the implementation of the KSW estimator for the ISW-lensing signal can be found in Mangilli et al. (2013). In particular, Eq. 16 takes the form

$$\hat{A}^{\text{T}\phi} = (F^{-1})(\hat{S}_{\text{cubic}} + \hat{S}_{\text{linear}}), \quad (18)$$

where \hat{S}_{cubic} is the term that extracts the amplitude information from the data contained in the bispectrum, while \hat{S}_{linear} is a zero-mean term that reduces estimator variance when the experimental setup breaks rotational invariance, i.e., in the presence of sky

cut and anisotropic noise. To estimate $\hat{A}^{T\phi}$ we used the KSW estimator with an implementation of the linear term truncated at ℓ_{\max} as described in [Munshi & Heavens \(2010\)](#) and [Planck Collaboration XXIV \(2013\)](#).

3.1.3. Binned bispectrum

The binned bispectrum estimator ([Bucher et al. 2010](#)) achieves the required computational reduction in determining $A^{T\phi}$ by binning Eq. 11. In particular, the maximally filtered maps in Eq. 10 are replaced by

$$T_i(\Omega) = \sum_{\ell \in \Delta_i} \sum_{m=-\ell}^{+\ell} a_{\ell m} Y_{\ell m}(\Omega), \quad (19)$$

where the Δ_i are suitably chosen intervals (bins) of multipole values (chosen in such a way as to minimize the variance of the quantities to be estimated). These maps are then used in Eq. 9 to obtain the binned observed bispectrum, and analogously for B^{lin} . The bispectrum template $B^{\text{lens-ISW}}$ and inverse-variance weights V are also binned by summing them over all ℓ values in the bin. Finally these binned quantities are inserted in the general expression for $A^{T\phi}$ (Eq. 11), with the sum over ℓ replaced by a sum over bin indices i . Since most bispectrum shapes change rather slowly (with features on the scale of the acoustic peaks, like the power spectrum), the binned estimator works very well, increasing the variance only slightly, while achieving an enormous computational reduction (from about 2000 multipoles in each of the three directions to only about 50 bins).

3.1.4. Modal bispectra

Modal decomposition of bispectra has been introduced by [Fergusson et al. \(2010\)](#) as a way to compute reduced bispectra that uses a diagonalization ansatz such that the shape function in Fourier space can be separated, which reduces the dimensionality of the integration. At the same time it greatly reduces the complexity of estimating bispectra from data. The separation of the bispectrum shape function into coefficients $q_p^\ell(x)$ allows the derivation of a filtered map $M_p(\hat{n}, x)$,

$$M_p(\hat{n}, x) = \sum_{\ell m} \frac{q_p^\ell(x) a_{\ell m}}{C_\ell} Y_{\ell m}(\hat{n}), \quad (20)$$

from the coefficients $a_{\ell m}$ of the temperature map. With that expression, one can obtain a mode expansion coefficient β ,

$$\beta_{prs} = \int d\Omega \int x^2 dx M_p(\hat{n}, x) M_r(\hat{n}, x) M_s(\hat{n}, x). \quad (21)$$

With that decomposition, the estimator of the bispectrum assumes a particularly simple diagonal shape,

$$\hat{S} = \frac{6}{N} \Delta_\Phi^2 \sum_{prs} \alpha_{prs} \beta_{prs}, \quad (22)$$

where the α_{prs} are the equivalent coefficients obtained by performing the modal decomposition of the theoretical bispectrum shape function. The relation between modal bispectra and wavelet bispectra is derived by [Regan et al. \(2013\)](#).

3.2. Results

The detection of the ISW effect via the non-Gaussian signal induced by the gravitational lensing potential is summarized in Table 2. We provide the estimates of the ISW-lensing amplitude $A^{T\phi}$, its uncertainty σ_A and the signal-to-noise obtained with the different estimator pipelines described in Sec. 3.1. The estimators have been applied to the official *Planck* CMB maps made using C-R, NILC, SEVEM, and SMICA ([Planck Collaboration XII 2013](#)). The quantity σ_A is obtained from 200 simulations representative of the analysed CMB data maps. These Monte Carlo simulations (FFP-6, see [Planck Collaboration I 2013](#)) account for the expected non-Gaussian ISW-lensing signal, according to the *Planck* best-fit model, and have been passed through the different component separation pipelines, as described in [Planck Collaboration XII \(2013\)](#). Lensed simulations can be found in [Planck Collaboration XVII \(2013\)](#). The mask used in the analysis is the combined Galactic and point source common mask (U73, [Planck Collaboration I 2013](#)) with sky fraction $f_{\text{sky}} = 0.73$.

The KSW and the $T\phi$ estimators show similar sensitivity, finding, respectively, $A^{T\phi} = 0.81 \pm 0.31$ and $A^{T\phi} = 0.70 \pm 0.28$ from the SMICA CMB map, which corresponds to a significance at about the 2.5σ level. The modal and binned estimators are slightly less optimal, but give consistent results, which is consistent with the imperfect overlap of the modal estimator templates with the ISW-lensing signal; the ISW-lensing bispectrum has a rapidly oscillating shape in the squeezed limit and both, binned and modal estimates, are better suited (and originally implemented) to deal with smooth bispectra of the kind predicted by primordial inflationary theories. Since the correlation coefficient of the binned and modal ISW-lensing templates relative to the actual ISW-lensing bispectrum (Eq. 8) is generally $0.8 < r < 0.9$ (to be compared with $r = 0.99$, achieved by both estimators for local, equilateral and orthogonal primordial templates, [Planck Collaboration XXIV 2013](#)), the corresponding estimator's weights are expected to be about 20 % suboptimal, consistent with observations.

The $T\phi$ estimator has also been applied to the specific *Planck* lensing baseline, i.e., the MV map, which is a noise-weighted combination of the 217 GHz and 143 GHz channel maps, previously cleaned from infrared contamination through subtraction of the 857 GHz map, taken as a dust template. From this map the lensing potential is recovered and then correlated with that potential field in order to estimate the amplitude $A^{T\phi}$. The official baseline adopts a more conservative high-pass filtering, such that as only multipoles $\ell \geq 10$ are considered, and the mask with $f_{\text{sky}} = 0.7$ is used. In this case, the ISW-lensing estimate is 0.78 ± 0.32 (a 2.4σ detection, where the error bars are obtained from 1000 simulations), as reported in the first sub-row for $T\phi$ in Table 2. The full multipole range is considered in the second sub-row, obtaining about 7% better sensitivity.

Notice that, according to all the estimators, the C-R CMB map provides lower significance for ISW-lensing, since its resolution is slightly lower than that of the other maps. NILC and SMICA exhibit a somewhat larger detection of the ISW signal, since they are the least noisy maps.

In order to explore the agreement among the different estimators, we performed a validation test based on 200 lensed simulations processed through the SMICA pipeline. The results are summarized in Table 3. For each pair of statistics, we provide the difference in amplitudes estimated for the data ($\Delta A^{T\phi}$), the dispersion of the difference of amplitudes obtained from the simulations (s_A), the ratio between this dispersion and the largest

Table 2. Amplitudes $A^{T\phi}$, errors σ_A and significance levels of the non-Gaussianity due to the ISW effect, for all component separation algorithms (C-R, NILC, SEVEM, and SMICA) and all the estimators (potential reconstruction, KSW, binned, and modal). For the potential reconstruction case, an additional minimum variance (MV) map has been considered (see [Planck Collaboration XVII 2013](#) for details).

Estimator	C-R	NILC	SEVEM	SMICA	MV
$T\phi$	$\ell \geq 10$	0.52 ± 0.33	1.5	0.72 ± 0.30	2.4
	$\ell \geq 2$	0.52 ± 0.32	1.6	0.75 ± 0.28	2.7
KSW		0.75 ± 0.32	2.3	0.85 ± 0.32	2.7
binned		0.80 ± 0.40	2.0	1.03 ± 0.37	2.8
modal		0.68 ± 0.39	1.7	0.93 ± 0.37	2.5
				0.60 ± 0.37	1.6
				0.77 ± 0.37	2.1

Table 3. For each pair of estimators we provide the mean difference among the amplitudes estimated from the data ($\Delta A^{T\phi}$), the dispersion of the differences between the amplitudes estimated from the simulations (s_A), the ratio of this dispersion to the larger of the corresponding sensitivities (η), and the correlation coefficient (ρ).

	KSW	binned	modal
$T\phi$	$\Delta A \pm s_A$	-0.11 ± 0.10	-0.21 ± 0.21
	η	0.32	0.56
	ρ	0.95	0.84
KSW	$\Delta A \pm s_A$		0.04 ± 0.19
	η		0.52
	ρ		0.86
binned	$\Delta A \pm s_A$		0.14 ± 0.15
	η		0.41
	ρ		0.92

of the corresponding sensitivities (η , according to Table 2), and the correlation coefficient (ρ). As can be seen from the Table, the agreement among estimators is good and the discrepancies are only around 0.5σ , which is the expected scatter, given the correlation between the weights of different estimators discussed above. Overall, the bispectrum estimators provide a larger value of the amplitude $A^{T\phi}$, as compared to the $T\phi$ estimator.

We have also explored the joint estimation of the two bispectra that are expected to be found in the data: the ISW-lensing; and the residual point sources. A detailed description of the non-Gaussian signal coming from point sources can be found in [Planck Collaboration XXIV \(2013\)](#). The joint analysis of these two signals performed with the KSW estimator, and the binned, and modal estimators has shown that the ISW-lensing amplitude estimation can be considered almost completely independent of the non-Gaussian signal induced by the residual sources, and that the two bispectra are nearly perfectly uncorrelated.

There is not a unique way of extracting a single signal-to-noise value from Table 2. However, all the estimators show evidence of ISW-lensing at about the 2.5σ level.

Finally, we estimate that the bias introduced by the ISW-lensing signal on the estimation of the primordial local shape bispectrum (Eq. 14) is $\Delta^{\text{prim}} \simeq 7$, corresponding to the theoretical expectation, as described in detail in [Planck Collaboration XXIV \(2013\)](#).

4. Cross-Correlation with surveys

The ISW effect can be probed through several different approaches. Among the ones already explored in the literature, the classical test is to study the cross-correlation of the CMB temperature fluctuations with a tracer of the matter distribution, typ-

ically a galaxy or cluster catalogue. As mentioned in the introduction, the correlation of the CMB with LSS tracers was first proposed by [Crittenden & Turok \(1996\)](#) as a natural way to amplify the ISW signal, otherwise very much subdominant with respect to the primordial CMB fluctuations. Indeed, this technique led to the first reported detection of the ISW effect ([Boughn & Crittenden 2004](#)).

Several methods have been proposed in the literature to study statistically the cross-correlation of the CMB fluctuations with LSS tracers, and, they can be divided into: real space statistics (e.g., the cross-correlation function, hereinafter CCF); harmonic space statistics (e.g., the cross-angular power spectrum, hereinafter CAPS); and wavelet space statistics (e.g., the covariance of the Spherical Mexican Hat Wavelet coefficients, or SMHWcov from now on). These statistics are equivalent (in the sense of the significance of the ISW detection) under ideal conditions. However, ISW data analysis presents several problematic issues (incomplete sky coverage, selection biases in the LSS catalogues, foreground residuals in the CMB map, etc.). Hence, the use of several different statistical approaches provides a more robust framework for studying the ISW-LSS cross-correlation, since different statistics may have different sensitivity to these systematic effects. The individual methods are described in more detail in Sect. 4.1.

Besides the choice of specific statistical tool, the ISW cross-correlation can be studied from two different (and complementary) perspectives. On the one hand, we can determine the amplitude of the ISW signal, as well as the corresponding signal-to-noise ratio, by comparing the observed cross-correlation to the expected one. On the other hand, we can postulate a null hypothesis (i.e., that there is no correlation between the CMB and the LSS tracer) and study the probability of obtaining the observed cross-correlation. Whereas the former answers a question regarding the compatibility of the data with the ISW hypothesis (and provides an estimation of the signal-to-noise associated with the observed signal), the latter tells us how incompatible the measured signal is with the no-correlation hypothesis, i.e., against the presence of dark energy (assuming that the Universe is spatially flat). Obviously, both approaches can be extended to account for the cross-correlation signal obtained from several surveys at the same time. These two complementary tests are described in detail in Sect. 4.2, with the results presented in Sect. 4.3.

4.1. Cross-correlation statistics

Let us denote the expected cross-correlation of two signals (x and y) by ξ_a^{xy} , where a stands for a distance measure (e.g., the angular distance θ between two points in the sky, the multipole ℓ of the harmonic transformation, or the wavelet scale R). For

simplicity, we assume that the two signals are given in terms of a fluctuation field (i.e., with zero mean and dimensionless).

This cross-correlation could represent either the CCF, the CAPS or the SMHWcov. It has to be understood as a vector of a_{\max} components, where a_{\max} is the maximum number of considered *distances*. Obviously, when $x \equiv y$, ξ_a^{xy} represents an auto-correlation. The specific forms for ξ_a^{xy} and $\mathbf{C}_{\xi^{xy}}$ for the different cross-correlation statistics (CAPS, CCF, and SMHWcov) are given below.

4.1.1. Angular cross-power spectrum

The angular cross-power spectrum (CAPS) is a natural tool for studying the cross-correlation of the CMB fluctuations and tracers of the LSS. Under certain conditions, it provides a statistical tool with uncorrelated (full-sky coverage) or nearly uncorrelated (binned spectrum for incomplete sky coverage) components. Even the unbinned CAPS, estimated on incomplete signals, can be easily worked out, since the correlations are mostly related to the geometry of the mask. This is the case for the CAPS obtained through MASTER approach (e.g., [Hivon et al. 2002](#); [Hinshaw et al. 2003](#)). Another approach is to work in the map domain, making use of a quadratic maximum likelihood (QML henceforth) estimator ([Tegmark 1997](#)) for the CAPS ([Padmanabhan et al. 2005](#); [Schiavon et al. 2012](#)). Such approach is optimal, i.e., leads to unbiased estimates for the CAPS with minimum error bars.

Pseudo angular power spectrum

Let us denote the CAPS between the CMB field $T(p)$ and an LSS tracer $G(p)$ map (where $p = (\theta, \phi)$ represents a given pixel) as: C_{ℓ}^{TG} (i.e., $\xi_a^{xy} \equiv C_{\ell}^{\text{TG}}$ for this cross-correlation estimator). In the full-sky case, an optimal estimator of the CAPS is given by:

$$\hat{C}_{\ell}^{\text{TG}} = \frac{1}{2\ell + 1} \sum_{m=-\ell}^{+\ell} t_{\ell m} g_{\ell m}^*, \quad (23)$$

where $t_{\ell m}$ and $g_{\ell m}$ are the spherical harmonic coefficients of the CMB and the LSS maps, respectively. This CAPS can be seen as a vector with ℓ_{\max} components, where ℓ_{\max} is the maximum multipole considered in the analysis. Here we adopt $3N_{\text{side}} - 1$, which suffices for ISW analysis, since it is known that most of the ISW signal is contained within $\ell \lesssim 80$ ([Afshordi 2004](#); [Hernández-Monteagudo 2008](#)). When a mask $\Pi(p)$ is applied to the maps, it acts as a weight that modifies the underlying harmonic coefficients. Now, we have $\tilde{t}_{\ell m}$ and $\tilde{g}_{\ell m}$, where

$$\begin{aligned} \tilde{t}_{\ell m} &= \int \int d(\cos \theta) d\phi T(\theta, \phi) \Pi(\theta, \phi) Y_{\ell m}^*(\theta, \phi), \\ \tilde{g}_{\ell m} &= \int \int d(\cos \theta) d\phi G(\theta, \phi) \Pi(\theta, \phi) Y_{\ell m}^*(\theta, \phi), \end{aligned} \quad (24)$$

and $Y_{\ell m}(\theta, \phi)$ are the spherical harmonic functions. In these circumstances, the estimator in Eq. 23 is no longer optimal, and is referred to as pseudo-CAPS. A nearly optimal estimator is given by decoupling the masked CAPS (denoted by $\tilde{C}_{\ell}^{\text{TG}}$) through the masking kernel B (e.g., [Xia et al. 2011](#)):

$$\tilde{C}_{\ell}^{\text{TG}} = B^{-1} \tilde{C}_{\ell}^{\text{TG}}, \quad (25)$$

where

$$B_{\ell \ell' G} = \frac{2\ell + 1}{4\pi} \sum_{\ell''} J_{\ell''}^G \left(\begin{array}{ccc} \ell & \ell' & \ell'' \\ 0 & 0 & 0 \end{array} \right)^2, \quad (26)$$

with $J_{\ell''}^G$ the cross-angular power spectrum of the T and G masks.

The estimator in Eq. 25 is nearly optimal because $\tilde{C}_{\ell}^{\text{TG}}$ has to be understood as the mean value over an ensemble average of skies. Let us point out that when more than a single CAPS is considered, for instance when one is interested in the cross-correlation of the *Planck* CMB map with more than one LSS tracer map, the CAPS estimator can be seen as a single vector with N_{\max} components, with N being the number of surveys.

It can be shown that the element $C_{\ell \ell' ij}$ of the covariance matrix of the CAPS estimator in Eq. 25 (for the case of a masked sky and for N surveys) is given by

$$C_{\ell \ell' ij} = K_{\ell,ij} K_{\ell',ij} \frac{(M_{ij})_{\ell \ell'}^{-1}}{(2\ell' + 1)}, \quad (27)$$

where

$$K_{\ell,ij} = \left[C_{\ell}^{\text{TG}_i} C_{\ell}^{\text{TG}_j} + C_{\ell}^{\text{T}} \left(C_{\ell}^{\text{G}_i \text{G}_j} + N_{\ell}^{\text{G}_i \text{G}_j} \delta_{ij} \right) \right]^{1/2}, \quad (28)$$

and $(M_{ij})_{\ell \ell'}^{-1}$ is the (ℓ, ℓ') element of the inverse matrix of M for surveys i and j fixed, such as

$$M_{\ell \ell' ij} = \frac{2\ell + 1}{4\pi} \sum_{\ell''} H_{\ell''}^{ij} \left(\begin{array}{ccc} \ell & \ell' & \ell'' \\ 0 & 0 & 0 \end{array} \right)^2, \quad (29)$$

Here $H_{\ell''}^{ij}$ is the angular cross-power spectrum of the two joint masks, i.e., the masks resulting from the multiplication of the T with G_i and G_j , respectively. The quantities C_{ℓ}^{xy} are expected or fiducial spectra, N_{ℓ}^{yy} is the Poissonian noise of the y survey (deconvolved by any beam or pixel filter), and δ_{ij} is the Kronecker delta. In Eq. 28, the instrumental noise associated with the CMB data has been ignored, since the *Planck* sensitivity is such that the noise contribution on the scales of interest is negligible. When more than one survey has poor sky coverage, then the complexity of the correlations is not well reflected by the previous expression. Therefore, in this paper, we will compute $C_{\ell \ell' ij}$ from coherent CMB and LSS Monte Carlo simulations. For each simulation, we generate four independent, Gaussian, and white realizations (at $N_{\text{side}} = 64$), which are afterwards properly correlated using the expected auto- and cross-correlations of the signals. Corresponding Poissonian shot noise realizations are added to each survey map. The resulting four maps are masked with the corresponding masks (i.e., one for the CMB and one for mask for each survey).

The computation of the CAPS in Eq. 25 is extremely fast (especially for the resolutions used in the study of the ISW). However, as stated above, it is only a *nearly* optimal estimator of the underlying CAPS. Moreover, its departure from optimality is largest at the smallest multipoles (largest scales), where the ISW signal is more important.

The QML angular power spectrum

The QML method for the power spectrum estimation of temperature CMB anisotropies was introduced by [Tegmark \(1997\)](#) and later extended to polarization by [Tegmark & de Oliveira-Costa \(2001\)](#). For an application to temperature and polarization to *WMAP* data see [Gruppuso et al. \(2009\)](#) and [Paci et al. \(2013\)](#). The same method was employed to measure the cross-correlation between the CMB and LSS in [Padmanabhan et al. \(2005\)](#), [Ho et al. \(2008\)](#), and [Schiavon et al. \(2012\)](#). The QML method is usually stated to be optimal, since it provides unbiased estimates and the smallest error bars allowed by the Fisher-Cramér-Rao inequality. As a drawback, from the computational

point of view, the QML is a very expensive approach. Let us denote the QML estimator of the CAPS between the CMB map T and an LSS tracer G (at multipole ℓ) by Q_ℓ^{TG} (i.e., $\xi_a^{\text{xy}} \equiv Q_\ell^{\text{TG}}$ for this cross-correlation estimator).

A detailed description of the algebra of the QML is given in Schiavon et al. (2012). We briefly recall here the basics of the CAPS estimator, which is given by:

$$\hat{Q}_\ell^{\text{TG}} = \sum_{\ell'X'} (F^{-1})_{\ell\ell'}^{\text{TG} X'} \left[\mathbf{x}^T \mathbf{E}_{\ell'}^{X'} \mathbf{x} - \text{Tr}(\mathbf{N} \mathbf{E}_{\ell'}^{X'}) \right], \quad (30)$$

where X represents any of the following spectra: $X = \{\text{T}, \text{TG}, \text{G}\}$. The vector \mathbf{x} has $2N_{\text{pix}}$ elements (with N_{pix} being the total number of pixels allowed by the joint CMB and LSS mask): the first set of N_{pix} corresponds to the CMB map, and the second one accounts for the LSS map. The $F_{\ell\ell'}^{\text{TG} X'}$ is the Fisher matrix defined as

$$F_{\ell\ell'}^{\text{TG} X'} = \frac{1}{2} \text{Tr} \left[\mathbf{C}^{-1} \frac{\partial \mathbf{C}}{\partial C_\ell^{\text{TG}}} \mathbf{C}^{-1} \frac{\partial \mathbf{C}}{\partial C_{\ell'}^{X'}} \right], \quad (31)$$

and the \mathbf{E} matrix is given by

$$\mathbf{E}_\ell^X = \frac{1}{2} \mathbf{C}^{-1} \frac{\partial \mathbf{C}}{\partial C_\ell^X} \mathbf{C}^{-1}. \quad (32)$$

The object $\mathbf{C} = \mathbf{S}(C_\ell^X) + \mathbf{N}$ is the global covariance matrix, including the signal \mathbf{S} and noise \mathbf{N} contributions, with C_ℓ^X being the fiducial theoretical angular power spectrum. The uncertainties in the QML estimates are given by the inverse of the Fisher matrix, which includes the correlation among different multipoles. The error associated with the shot noise of the galaxy surveys is modelled in the galaxy submatrix of \mathbf{N} .

The results presented on this paper are based on \hat{C}_ℓ^{TG} , whereas \hat{Q}_ℓ^{TG} is used as a cross-check, applied to a lower resolution version of the maps of $N_{\text{side}} = 32$. In addition the maximum multipole considered in this case is $\ell_{\text{max}} = 2N_{\text{side}}$, which has been already verified as a conservative limit for the QML.

4.1.2. Cross-correlation function

The cross-correlation function (CCF) is a suitable tool for studying the ISW effect via cross-correlation of the CMB fluctuations and tracers of the LSS, and it has been one of the most extensively used in this context (e.g., Boughn & Crittenden 2002; Giannantonio et al. 2008; Xia et al. 2009). On the one hand, the signal only appears at very large scales and, therefore, it is sufficient to work at resolutions at which the low performance of the CCF (in terms of computational time) is not a serious handicap. On the other hand, neither the CMB nor the LSS data are available with full sky coverage and, in some cases, the geometry of the masks is very complicated: the CCF adapts perfectly to the effects of partial sky coverage, since it is defined in real space. As a drawback, the Poissonian noise of the galaxy tracer appears at the smallest angular scales, where the signal-to-noise of the ISW effect is higher for this estimator. Therefore, a proper characterization of the shot noise is especially important for the CCF, in order to obtain a good estimation of the uncertainties.

Let us denote the CCF between the CMB map T and an LSS tracer G (at an angular distance of θ) as $C^{\text{TG}}(\theta)$ (i.e., $\xi_a^{\text{xy}} \equiv C^{\text{TG}}(\theta)$ for this cross-correlation statistic). The CCF estimator is defined as

$$\hat{C}^{\text{TG}}(\theta) = \frac{1}{N_\theta} \sum_{i,j} T_i G_j, \quad (33)$$

where the sum runs over all pixels with a given angular separation. For each angular bin centred around θ , N_θ is the number of pixel pairs separated by an angle within the bin. Only the pixels allowed by the joint CMB and LSS mask are considered. The angular bins used in this work are: $\theta_1 \in [0, 1]^\circ$; $\theta_2 \in (1, 3]^\circ$; $\theta_3 \in (3, 5]^\circ$; ...; and $\theta_{61} \in (119, 121]^\circ$. The choice of binning does not affect the results significantly.

The covariance of the CCF estimator can be easily derived from the one already computed for the CAPS in Eq. 27. It is sufficient to know that the CCF can be expressed in terms of the CAPS as

$$C^{\text{TG}}(\theta) = \sum_{\ell=0}^{\ell_{\text{max}}} \frac{2\ell+1}{4\pi} C_\ell^{\text{TG}} P_\ell(\cos \theta), \quad (34)$$

where $P_\ell(\cos \theta)$ are the Legendre polynomials. Hence, it is straightforward to prove that the covariance between the θ and θ' components of the CCF for the surveys i and j , respectively, is given by

$$C_{\theta\theta',ij} = \sum_{\ell} \sum_{\ell'} \frac{(2\ell+1)}{4\pi} \frac{(2\ell'+1)}{4\pi} P_\ell(\cos \theta) P_{\ell'}(\cos \theta') C_{\ell\ell',ij}. \quad (35)$$

4.1.3. Wavelet covariance

Wavelets provide an interesting alternative to more traditional tools (e.g., CCF or CAPS) for studying the CMB-LSS correlation. They exploit the fact that the ISW signal is mostly concentrated at scales of a few degrees (e.g., Afshordi 2004). Wavelets are ideal kernels to enhance features with a characteristic size, since the wavelet analysis at an appropriate scale R amplifies those features over the background. Therefore, wavelets could provide most of the signal-to-noise of the ISW effect by just analysing a narrow range of scales. They were first proposed for the ISW detection by Vielva et al. (2006), where the Spherical Mexican Hat Wavelet (SMHW, Martínez-González et al. 2002) was proposed as the filtering kernel. The basic idea of this approach is to estimate the covariance of the SMHW coefficients (SMHWcov) as a function of the wavelet scale (see e.g., Vielva et al. 2006, for details). Other wavelet kernels can be considered, such as needlets (Pietrobon et al. 2006a), directional wavelets (McEwen et al. 2007), or steerable wavelets (McEwen et al. 2008).

Let us denote the SMHWcov between the CMB map T and a LSS tracer G (at a wavelet scale R) as $\Omega^{\text{TG}}(R)$, i.e., $\xi_a^{\text{xy}} \equiv \Omega^{\text{TG}}(R)$ for this cross-correlation statistic. The SMHWcov estimator is defined as

$$\hat{\Omega}^{\text{TG}}(R) = \frac{1}{N_{\text{pix}}} \sum_i \omega_T(R) \omega_G(R), \quad (36)$$

where $\omega_T(R)$ and $\omega_G(R)$ are the SMHW coefficients for the CMB and the LSS at scale R , respectively (note that wavelet coefficients are forced to have zero mean on the observed sky). The scales considered in our study are $R = \{60, 90, 120, 150, 200, 250, 300, 350, 400, 500, 600\}$ in arcminutes.

As for the CCF, the covariance of the SMHWcov estimator can be easily derived from the one already computed for the CAPS in Eq. 27. It is sufficient to know that the SMHWcov can be expressed in terms of the CAPS as

$$\Omega^{\text{TG}}(R) = \sum_{\ell=0}^{\ell_{\text{max}}} \frac{2\ell+1}{4\pi} C_\ell^{\text{TG}} \omega_\ell^2(R), \quad (37)$$

where $\omega_\ell(R)$ is the SMHW window function at the scale R . Hence, it is straightforward to prove that the covariance between the R and R' components of the SMWHcov for surveys i and j , respectively, is given by:

$$C_{RR',ij} = \sum_{\ell} \sum_{\ell'} \frac{(2\ell+1)}{4\pi} \frac{(2\ell'+1)}{4\pi} \omega_\ell^2(R) \omega_{\ell'}^2(R') C_{\ell\ell',ij}. \quad (38)$$

4.2. Cross-correlation tests

For any of the cross-correlation estimators described above, we aim two different statistical tests. First, if the observed cross-correlation is given by $\hat{\xi}_a^{xy}$, then, a simple χ^2 can be proposed to estimate the amplitude A , such that $A\hat{\xi}_a^{xy}$ is the closest solution to $\hat{\xi}_a^{xy}$:

$$\chi^2(A) = [\hat{\xi}_a^{xy} - A\hat{\xi}_a^{xy}]^T C_{\xi^{xy}}^{-1} [\hat{\xi}_a^{xy} - A\hat{\xi}_a^{xy}], \quad (39)$$

where $C_{\xi^{xy}}$ is the covariance matrix (of dimension $a_{\max} \times a_{\max}$) of the expected cross-correlation ξ_a^{xy} , i.e., $C_{\xi^{xy}_{i,j}} \equiv \langle \hat{\xi}_{a_i}^{xy} \hat{\xi}_{a_j}^{xy} \rangle$. It is straightforward to show that the best-fit amplitude A and its dispersion are given by

$$A = [\hat{\xi}_a^{xy}]^T C_{\xi^{xy}}^{-1} \xi_a^{xy} \left[[\hat{\xi}_a^{xy}]^T C_{\xi^{xy}}^{-1} \hat{\xi}_a^{xy} \right]^{-1}, \quad (40)$$

$$\sigma_A = \left[[\hat{\xi}_a^{xy}]^T C_{\xi^{xy}}^{-1} \hat{\xi}_a^{xy} \right]^{-1/2}.$$

An analogy with Eq. 39 can be defined for the null hypothesis case:

$$\chi^2_{\text{null}} = [\hat{\xi}_a^{xy}]^T D_{\xi^{xy}}^{-1} \hat{\xi}_a^{xy}, \quad (41)$$

where $D_{\xi^{xy}}$ is the covariance of the cross-correlation of the two signals, in the absence of an intrinsic dependence, i.e., when $\xi_a^{xy} \equiv 0$. The ISW signal is very weak and, therefore it is a good approximation to assume that that $D_{\xi^{xy}} \approx C_{\xi^{xy}}$.

For Gaussian statistics, χ^2_{null} already provides the direct probability of the observed cross-correlation $\hat{\xi}_a^{xy}$ under the null hypothesis. However, several non-idealities (sky coverage, systematics, foregrounds residuals, etc.) forces us to use alternative approaches to estimate the probability. One of the most common options is to perform the cross-correlation of survey signal y with realistic simulations of the CMB, x , and compute a joint statistics (e.g., χ^2_{null}) for each simulation. The probability value associated with the data will come then be the fraction of simulations having a value of χ^2_{null} equal to or larger than the one obtained for the data. Both, $C_{\xi^{xy}}$ and $D_{\xi^{xy}}$ can be derived either analytically or numerically (via simulations).

The latter approach is computationally expensive, but, in some cases, could provide a more accurate defence against certain systematics, in particular the incomplete sky coverage. There are several options to perform such kind of simulations. The standard approach is the one mentioned above, i.e., cross-correlation of the LSS map with CMB simulations. This is a very robust approach, since it is usually hard to reproduce the systematics present in the LSS tracers, but incomplete because the LSS is fixed, resulting in a lack of randomness. An alternative method is to use a jack-knife test, which unfortunately tends to underestimate the errors. Finally, one can produce simulations of both the CMB and the LSS, assuming perfect knowledge of the properties of both signals, in particular of the LSS field (which, as mentioned above, is almost never the case). Comprehensive discussions of these approaches are given in [Cabré et al. \(2007\)](#) and [Giannantonio et al. \(2008\)](#).

Table 4. Expected significance A/σ_A of the CMB-LSS cross-correlation. Values obtained from each survey independently, as well as jointly, are given for all the estimators (CAPS, CCF, and SMHWcov).

$\hat{\xi}_a^{xy}$	NVSS	SDSS	CMASS/LOWZ	SDSS MG	all
CAPS	3.0	1.9	0.6	3.2	
CCF	3.0	1.9	0.6	3.1	
SMHWcov	3.0	1.9	0.5	3.1	

4.3. Results

In this section we present the results obtained from the cross-correlation of the galaxy catalogues described in Sect. 2.2 (NVSS, SDSS-CMASS/LOWZ and SDSS-MG) with the four *Planck* CMB maps presented in Sect. 2.1.1 (C-R, NILC, SEVEM, and SMICA). All these maps are analysed at a HEALPix resolution of $N_{\text{side}} = 64$. The cross-correlation estimators described in the previous section are applied to all cases. This comprehensive analysis will help to achieve a robust estimation of the ISW.

As already mentioned the covariance among all the components of the estimators are obtained from coherent Gaussian simulations of the CMB and the three galaxy catalogues. Since we are only considering large-scale effects (above about 1°), the same set of CMB simulations are equally valid for the four CMB maps, since they are nearly identical on such scales (see [Planck Collaboration XII 2013](#), for details). We have used 70,000 coherent Monte Carlo simulation sets (as described in Sect. 4.1.1) to compute the correlations; this is enough to characterize the covariance.

The expected signal-to-noise ratio for the ISW effect detection is summarized in Table 4. Values for all the cross-correlation estimators are given. We consider the case of a survey-by-survey detection, as well as the joint analysis of all the surveys. A signal-to-noise of about 3σ is expected for the joint analysis, which is actually dominated by the NVSS cross-correlation. This is expected, since, firstly, NVSS covers a much larger fraction of the sky compared to other surveys, and secondly, it extends over a redshift interval ideal for the detection of the ISW signal (e.g. [Afshordi 2004](#)).

The differences among estimators are not significant, indicating that none of them is clearly optimal compared with the others. To explore this agreement further, we have analysed an extra set of 1,000 CMB and LSS clustered simulations, and have compared, simulation by simulation, the ISW amplitude estimation derived for each cross-correlation estimator (C_ℓ^{TG} , $C^{\text{TG}}(\theta)$ and $\Omega^{\text{TG}}(R)$). In Table 5 we summarize the comparison. We only report values for the joint fit to the ISW amplitude for the three surveys. Similar results are found survey by survey. For each pair of estimators, we provide the mean difference among the amplitude estimations (ΔA), the dispersion of these differences (s_A), the ratio (η) of this dispersion to the expected sensitivity (i.e., the inverse of the signal-to-noise numbers given in the last column of Table 4), and the correlation coefficient (ρ). It is clear that the agreement between estimators is very high and that differences are, on average, lower than half the statistical uncertainty imposed by the sampling variance.

We have fitted the observed cross-correlations to the expected ISW signal (C_ℓ^{TG} , $C^{\text{TG}}(\theta)$, and $\Omega^{\text{TG}}(R)$, see Fig. 5), following Eq. 41, i.e., allowing for a free amplitude of the expected signal. Results are summarized in Table 6. Overall, the ISW detection is at about the 3σ level and, as expected, it is clearly

Table 6. Amplitudes A , errors σ_A and significances A/σ_A of the CMB-LSS cross-correlation (survey by survey and all together) due to the ISW effect, for all component separation algorithms (C-R, NILC, SEVEM, and SMICA) for the CAPS, CCF, and SMHWcov estimators.

LSS data	$\hat{\xi}_a^{xy}$	C-R	NILC	SEVEM	SMICA
NVSS	CAPS	0.86 ± 0.33	2.6	0.91 ± 0.33	2.8
	CCF	0.80 ± 0.33	2.4	0.84 ± 0.33	2.5
	SMHWcov	0.89 ± 0.34	2.6	0.93 ± 0.34	2.8
SDSS-CMASS/LOWZ	CAPS	0.98 ± 0.52	1.9	1.09 ± 0.52	2.1
	CCF	0.81 ± 0.52	1.6	0.91 ± 0.52	1.8
	SMHWcov	0.80 ± 0.53	1.5	0.89 ± 0.53	1.9
SDSS-MG	CAPS	1.31 ± 0.57	2.3	1.43 ± 0.57	2.5
	CCF	1.00 ± 0.57	1.8	1.11 ± 0.57	2.0
	SMHWcov	1.03 ± 0.59	1.8	1.18 ± 0.59	2.0
all	CAPS	0.84 ± 0.31	2.7	0.91 ± 0.31	2.9
	CCF	0.77 ± 0.31	2.5	0.83 ± 0.31	2.7
	SMHWcov	0.86 ± 0.32	2.7	0.92 ± 0.32	2.9

Table 5. For each pair of estimators we provide the mean difference among the amplitude estimations (ΔA), the dispersion of these differences (s_A), the ratio (η) of this dispersion to the expected sensitivity (i.e., the inverse of the signal-to-noise numbers given in the last column of Table 4), and the correlation coefficient (ρ).

	CCF	SMHWcov
CAPS	$\Delta A \pm s_A$	-0.01 ± 0.12
	η	0.36
	ρ	0.93
CAPS	$\Delta A \pm s_A$	0.08 ± 0.14
	η	0.42
	ρ	0.92

dominated by the NVSS signal. There are only small differences among estimators and CMB maps (as expected from the above discussion), indicating that this is a robust result. Notice that all the estimated amplitudes are compatible with unity, within the error bars (especially for NVSS and SDSS-CMASS/LOWZ). This is an additional validation of how CMB and LSS are modelled. Values of A deviating significantly from unity would indicate some tension between the observed cross-correlation and the model (in particular on the LSS modelling, which is more complex). The CAPS-QML, applied to the SEVEM and NVSS (i.e., the survey with the highest signal-to-noise), yields a value of $A = 0.73 \pm 0.33$, which is compatible with the CAPS, when applied to the same $N_{\text{side}} = 32$ and $\ell_{\text{max}} = 2N_{\text{side}}$ resolution ($A = 0.84 \pm 0.34$). Preliminary tests indicate that running the CAPS-QML at $N_{\text{side}} = 64$ resolution could increase the sensitivity for detecting the ISW effect with NVSS by $\approx 20\%$.

Our results indicate a somewhat smaller signal-to-noise with respect to some previous analyses on *WMAP* data, where several (and in some case quite similar) surveys were also considered. For instance, Ho et al. (2008) and Giannantonio et al. (2012) found 3.7σ and 4.4σ detections, respectively. Compatibility with the former is below 1σ , whereas there is more tension (around 1.5σ) with the latter. A fraction of around 0.3σ of these differences could be explained in terms of the cosmological parameters adopted to define the theoretical expectations. In particular, the lower values of H_0 and Ω_Λ found by *Planck* (*Planck*

Collaboration XVI 2013) with respect to *WMAP* (e.g., Larson et al. 2011), imply a sensitivity for the ISW $\approx 10\%$ smaller. The rest of the differences come either from the LSS side, or from the error characterization, which depends on the presence of a correlated signal between CMB and LSS simulations (see for instance Cabré et al. 2007, for a discussion). Survey modelling is another important aspect: besides systematic errors associated with the galaxy identification and redshift estimation procedures, there are complicated aspects, such as the bias characterization. As was mentioned already, a strong point of our results, is the excellent compatibility between the ISW amplitude estimates with respect to the expected value. Whereas our estimation deviates by about 0.5σ from the expected value, the Giannantonio et al. (2012) result exceeds it by about 1σ and Ho et al. (2008) is around 2σ above.

Nevertheless, the value of the ISW effect that we measure by means of NVSS (that because of its large sky coverage, redshift range, and density of galaxies is probably the best current catalogue for studying the ISW effect) is significant, and in agreement with previously published results using *WMAP*.

We have also studied the ISW signal from the point of view of its compatibility with the null hypothesis. We have considered in this analysis only the NVSS catalogue, since it provides the largest detection of the ISW effect and, therefore, is the best of the existing surveys for challenging the null hypothesis. Probability values are summarized in Table 7. As mentioned in Sect. 4.2, there is not a unique way of computing the null hypothesis. Our approach follows Eq. 41, where $D_{\xi^{xy}}$ was computed out of 90,000 CMB simulations that have been cross-correlated with the LSS data. This matrix is used to compute χ^2_{null} from the data. This value is then compared to its distribution for the null hypothesis, obtained from 1,000 realistic CMB simulations (FFP-6) uncorrelated with NVSS, which have been processed in the same way as the *Planck* data set. CAPS provides the smallest probability value, but the null hypothesis is rejected at about 10% only; this result is not unexpected, since an expected result since the ISW effect is weak.

The fact that the CAPS statistic provides tighter limits with respect to the CCF and SMHWcov could have been anticipated. In our implementation, the CAPS explores the maximum angular range allowed for a given map, whereas the CCF and the SMHWcov approaches are only evaluated at certain angles/scales. This limitation is not an issue in the analysis devoted

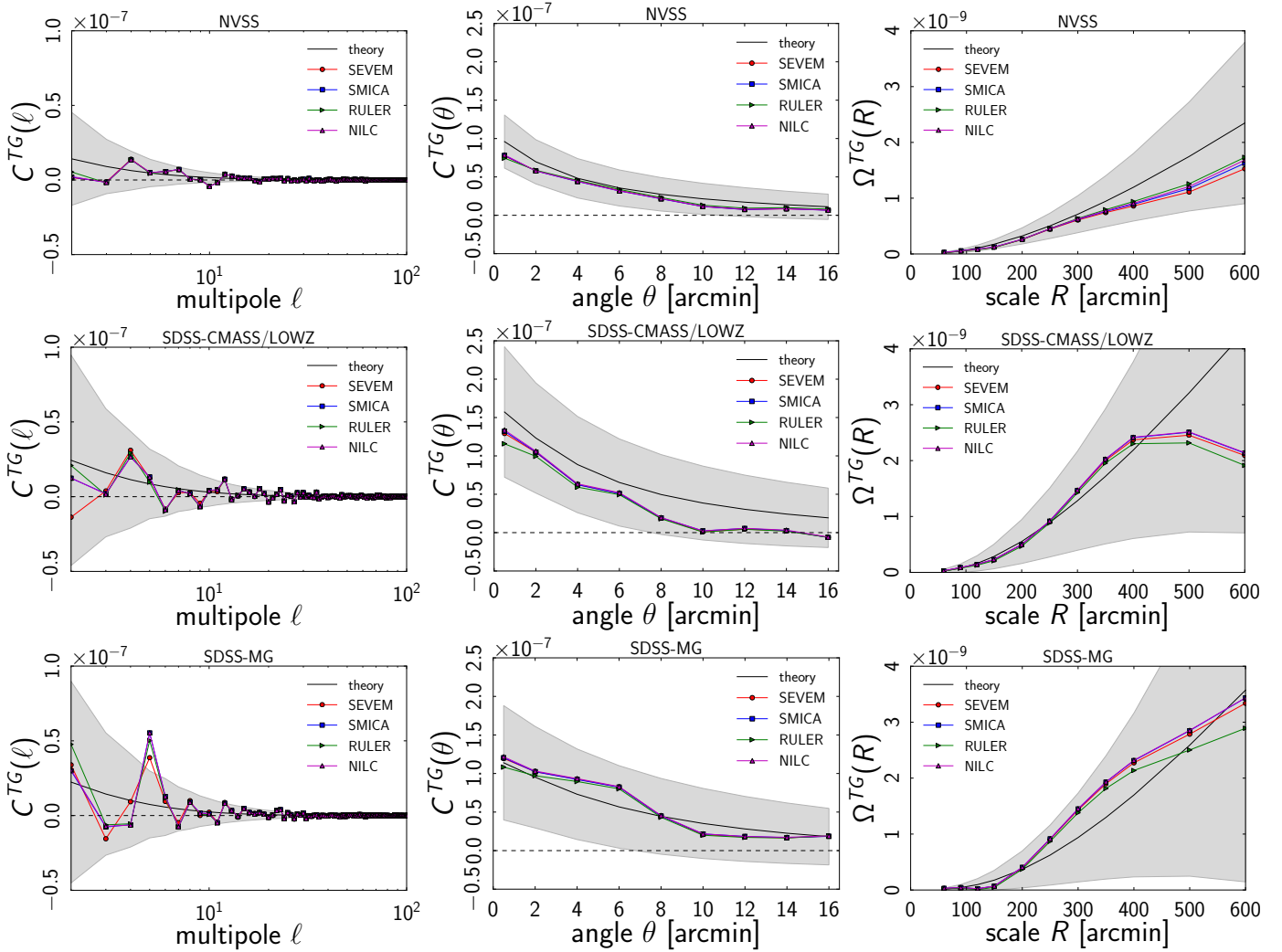


Fig. 5. Observed and expected cross-correlation signal versus multipole ℓ , for several surveys and different cross-correlation estimators. Columns from left to right correspond to: CAPS; CCF; and SMHWcov. Rows from top to bottom represent: NVSS; SDSS-CMASS/LOWZ; and SDSS-MG. On each panel we show the expected cross-correlation (black line) and the $\pm 1\sigma$ region (grey area). Observed cross-correlations for the different CMB maps are provided: C-R and NILC as green and magenta triangles, respectively; SEVEM as red circles; and SMICA as blue squares.

Table 7. Probability values of the CMB-LSS cross-correlation for the NVSS survey under the null hypothesis, for the four component separation methods (SMICA, SEVEM, C-R and NILC) and for the CAPS, CCF, and SMHWcov estimators.

LSS data	$\hat{\xi}_a^{xy}$	C-R	NILC	SEVEM	SMICA
NVSS	CAPS	0.09	0.10	0.10	0.09
	CCF	0.33	0.34	0.40	0.33
	SMHWcov	0.20	0.23	0.27	0.19

to estimating the ISW amplitude, since these angles/scales are suitable for detecting the ISW. However, in order to discard the null hypothesis, the longer the number of “distances” the better.

5. Stacking of large-scale structures

An alternative approach for measuring the ISW effect in *Planck* maps is to look for an ISW signal directly at the positions of positive and/or negative peaks in the potential. Since the ex-

pected (and observed) signal is very weak, for individual structures, a stacking technique needs to be applied. Using the *WMAP* data, it has been shown that CMB maps show hot spots and cold spots in the direction of superclusters and supervoids, respectively (Granett et al. 2008a,b, GR08 hereafter), which appear to be barely consistent with the predictions of standard Λ CDM (see also Hernandez-Monteagudo & Smith 2012). These structures, which are not yet virialized, are evolving while the CMB photons travel across them and this should contribute to the ISW effect. We apply here the same approach to the different *Planck* maps, using the catalogues of superstructures introduced in Sect. 2.2.4, and we test for the robustness of our findings. We first discuss our method and the results obtained using the catalogue provided by GR08, and then present the results obtained with the other catalogues.

5.1. Method

Our analysis is performed on the SMICA CMB map, although we have checked that results are compatible for the other three

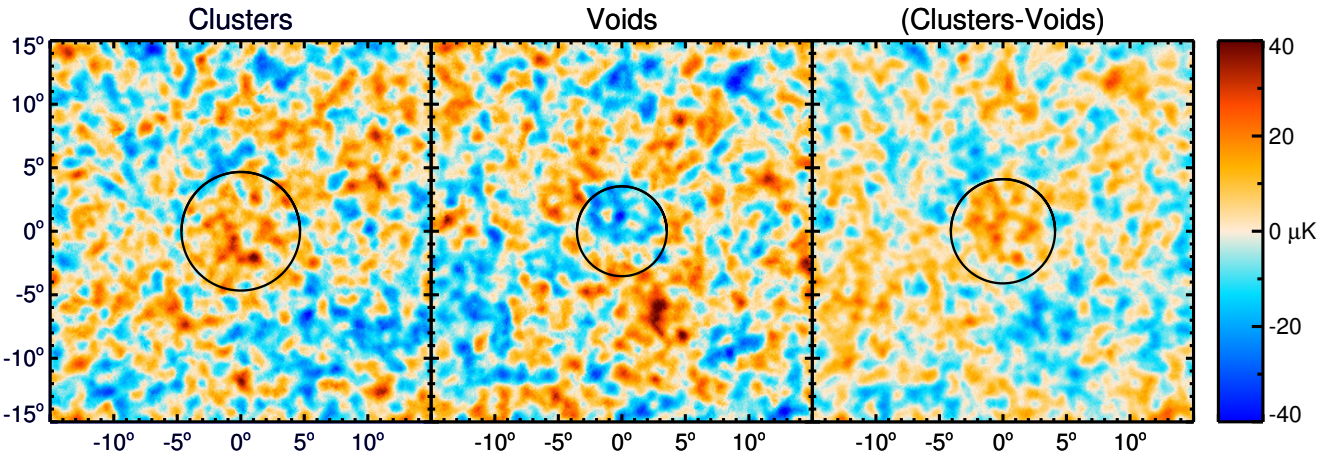


Fig. 6. Stacked regions of *Planck* maps corresponding to the locations of the superstructures identified by GR08. From left to right we show the images resulting from stacking of the 50 superclusters, the 50 supervoids, and the difference of both. The black circles superimposed indicate the angular radius at which the signal-to-noise ratio is maximal. See Fig. 7 for the corresponding temperature and photometry profiles, as well as their statistical significance.

Planck maps. We have also used the cleaned frequency maps from SEVEM (see Sect. 2.1.1) for some of the tests. We first remove the monopole and dipole of the maps (outside the U73 mask), and then apply a compact source mask based on the Planck Legacy Point Source Catalogue (Planck Collaboration XII 2013) to remove the contamination from individual point sources.

For the purpose of comparison with the results of GR08, we smooth the CMB maps with a common Gaussian kernel of $30'$ FWHM. We then project them onto patches around each position in the supervoid and supercluster catalogue. The GR08 structures have a relatively small size on the sky (a few degrees), but the other two catalogues considered here contain many larger and closer voids, covering larger angular sizes. Thus we work with $30^\circ \times 30^\circ$ CMB patches and choose the pixel size to be $6'$, so that all voids considered are fully enclosed. We then co-add (stack) the maps, taking into account the mask used. On the stacked images, we calculate both the radial temperature profile and the aperture photometry, to characterize the signal around density structures. The temperature profile is obtained by computing the mean of the pixels in rings of fixed width and increasing angular radius; in practice, it is calculated for 150 radii between 0° and 15° , with a width of $\Delta\theta = 0^\circ.1$. The photometry profile is obtained by applying a compensated filter that subtracts the average temperature of a ring from the average temperature within the disk whose radius θ is the inner radius ring, and where the outer radius is chosen to be $\theta\sqrt{2}$, so that the disc and ring have the same area. This should enhance fluctuations of typical angular size θ against fluctuations at smaller or larger scales. Aperture photometry results are also provided for 150 angles, this time between 0° and $15/\sqrt{2} \approx 10^\circ.6$. In addition to the monopole and dipole, we also removed from the CMB maps the contribution of large scale angular modes, namely $\ell = 2\text{--}10$. These modes correspond to angular scales much larger than those of the structures under investigation, and for our purposes their only effect is to introduce gradients in the stacked images; the high-pass filter essentially stops such gradients getting into the stacked map (which is equivalent to removing gradients at the end). The contribution of the large-scale angular modes has no impact on the aperture photometry profiles, and introduces only an offset in the temperature profiles (Ilić et al. 2013).

In order to estimate the significance of the resulting photometry and temperature profiles, we follow a Monte Carlo approach based on stacked CMB images chosen at random positions. In detail, we compute the photometry and the temperature profiles for 16 000 sets of 50 CMB patches randomly distributed over the SDSS area. We then compare the profiles obtained from the stacking at the location of the GR08 superstructures to these random profiles, in order to compute their signal-to-noise ratio.

5.2. Results

We show in Fig. 6 the stacked images of the 50 supervoids and 50 superclusters of GR08 in the *Planck* map. The corresponding temperature and photometry profiles, along with their significance levels, are shown in Fig. 7. The first thing to say is that, although the signatures are fairly weak, the sign of the effect certainly seems to be correct. Using the same catalogue and the *Planck* CMB map, we find reasonable agreement with GR08. The maximal photometric decrement, $-10.8\,\mu\text{K}$ (essentially identical with the $-11.3\,\mu\text{K}$ found by GR08), induced by supervoids is obtained for a preferred scale of about 3.5 (4° in GR08) and a signal-to-noise of 3.3 ($3.7\,\sigma$ in GR08), as shown in Fig. 7. Superclusters produce a photometric increment of about $8.5\,\mu\text{K}$ (slightly above the $7\,\mu\text{K}$ in GR08), with a significance of $3.0\,\sigma$ (compared with $2.6\,\sigma$ in GR08) at a slightly larger angle of 4.7° . Finally, the stack of the combined sample (clusters minus voids) gives a temperature deviation of $8.7\,\mu\text{K}$, with a signal strength of $4.0\,\sigma$ at 4.1° , which is consistent with the values reported in GR08. The values of statistical significance for our aperture aperture photometry results are closely related to those for the temperature profiles. Indeed, as shown in the top panel of Fig. 7, the temperature profile for the void stack shows a roughly $2\,\sigma$ deficit at small angular radii and a roughly $2\,\sigma$ excess extending to large radii. Since the aperture photometry is essentially an integral of the temperature profile with a compensated filter, it picks up enhanced significance because of the shape of the temperature profile.

As noted previously by several authors (e.g., Hernandez-Monteagudo & Smith 2012), the amplitude and shape of the photometric profile found for voids and clusters is in tension (around $2\,\sigma$) with the values expected from pure ISW within ΛCDM .

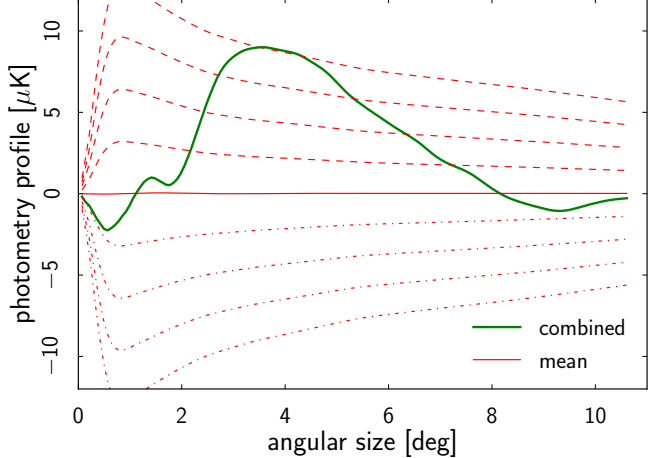
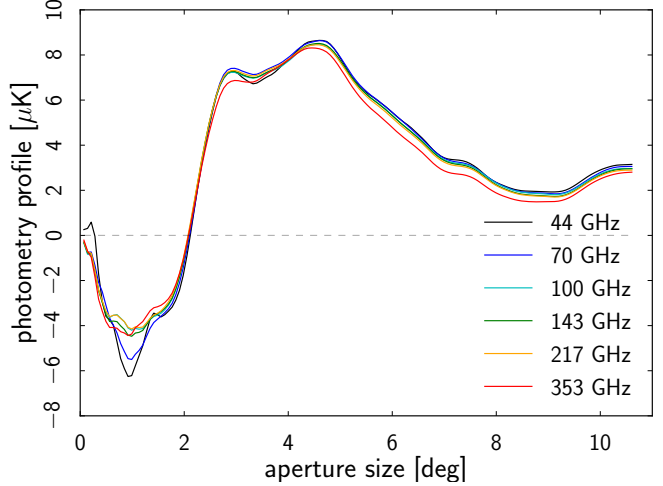
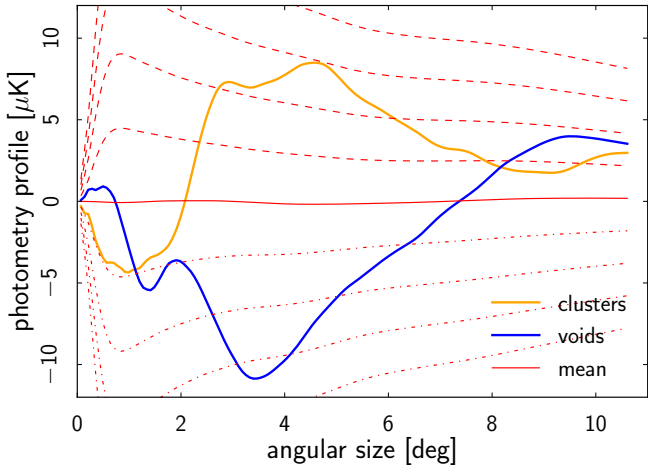
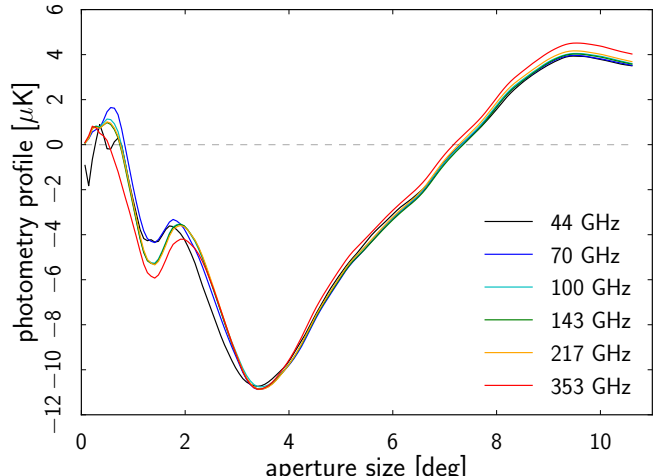
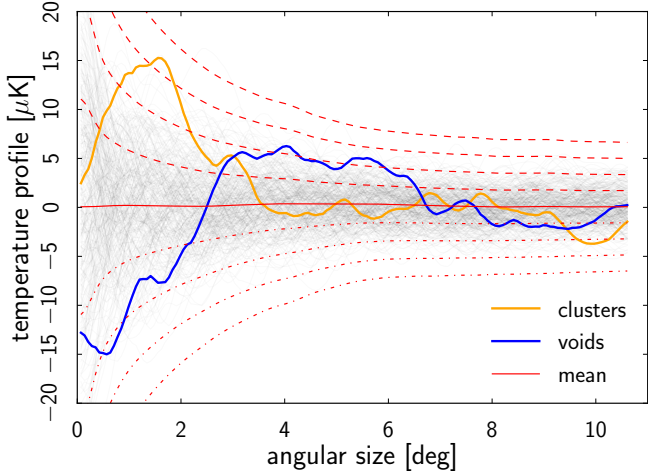


Fig. 7. Temperature (top) and photometry (middle and bottom) profiles of the stacked CMB patches at the location of the 50 supervoids and 50 superclusters of GR08. The lower panel shows the combined photometry profile (i.e., the average cluster profile minus the average void profile). The significance is represented by 1, 2, 3, and 4σ level curves (dashed and dotted lines represent positive and negative error bars, respectively). These curves represent the dispersion of the 16 000 stacks of 50 CMB patches chosen at random positions (for illustration, on the top panel, we represent in grey 300 of those random profiles).

However, it is not straightforward to associate this entire signal

Fig. 8. Independence of the signal on the SEVEM frequency channels. The aperture photometry profiles measured in the stacked patches centred on supervoids (top) and superclusters (bottom) are virtually identical for all frequencies.

with a pure ISW effect. As seen in the Fig. 6, many small-scale structures – both cold and hot – are present around the region delineated by the angular radius at which the signal-to-noise ratio of the aperture photometry is maximal. This small-scale structure contributes to the amplitude of the photometric decrement, but at a few tens of μK , which is incompatible with the ΛCDM predictions for the ISW effect. These are rather simply background CMB fluctuations, with their lingering presence due to the small number (50) of patches which are used to produce the stack.

It is intriguing that the angular sizes of the catalogued superstructures are smaller than the angular sizes suggested by the photometry profiles. This result is more apparent when we repeat the stacking analysis after rescaling each CMB patch by the effective radius of the structure it contains. Since the voids and super clusters identified by GR08 are roughly the same size, the photometric results are similar after rescaling ($-10 \mu\text{K}$ for voids and $7.9 \mu\text{K}$ for superclusters). However, the deviations have significance levels of 3.3σ and 2.7σ for supervoids and superclusters, respectively, at angular sizes of 1.3 (voids) and 2.6 (clusters) times the effective radius of the structures. This mismatch could be a result of underestimation of the structure extent the ZOBOV and VOBOZ algorithms (as already suggested by GR08) or

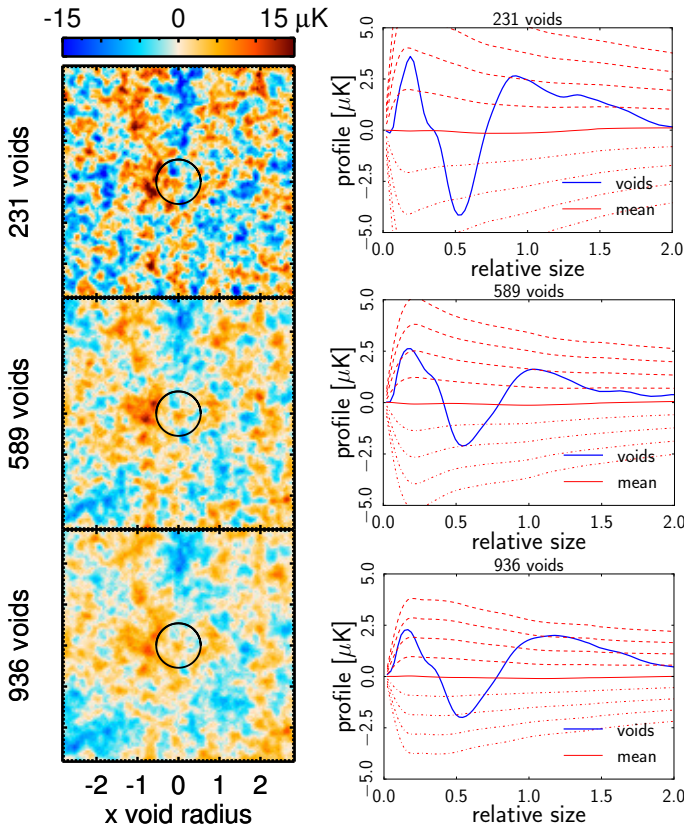


Fig. 9. Stacked images (left) and photometry profiles (right) obtained for the voids of Sutter et al. (2012). From top to bottom, we show results obtained from stacking the largest 231, 589, and 936 voids. The black circles superimposed indicate the angular radius at which the signal is maximal. The statistical dispersion is reduced as we stack more voids. However, the amplitude of the “cold spot” at about 0.5 times the effective void radius is mostly due to the surrounding “hot shell”, which is easiest to see in the bottom panel. This is further demonstrated by the 3σ signal detected using aperture photometry, seen at radii above 1.2 times the effective radius (for the 936 void case). Dashed and dotted lines in the right-hand panels represent positive and negative error bars, respectively, from 1 to 4σ .

because larger potential hills and valleys underlie the detected superstructures. Since structure in the potential is related to the density field through the Poisson equation, gravitational potential features are expected to cover larger scales than structures in the density field. Nevertheless, the factor of 2.6 for the case of superclusters seems large. It is also true that the GR08 superstructures were identified in the LRG subsample of the SDSS, and LRGs are known to be biased tracers of the matter density field (e.g., Tegmark et al. 2006). This bias could help explain why structures are larger than the scales identified by the VOBOZ algorithm, although the argument would go in the opposite sense for the voids. Another way of stating this is (Hunt & Sarkar 2010) that the relatively large effect decrement found for the GR08 voids can be only be attributed to the ISW effect only if the underdensities have been significantly underestimated or if the LRGs are under-biased.

It is therefore difficult to be confident that the signal is due entirely to the ISW effect. We know, however, that the ISW signal generated by superstructures is expected to be achromatic,

since it generates a fractional perturbation of the CMB temperature. In order to check if the signal we measure is indeed independent of frequency, we applied the same technique to *Planck* individual SEVEM cleaned frequency maps from 44 to 353 GHz. Lower (higher) frequency maps may be contaminated by radio (IR) signals coming from our Galaxy and may thus introduce a bias in the measurement. Figure 8 shows the photometry profiles of supercluster- and supervoid-stacked maps at 44, 70, 100, 143, 217, and 353 GHz. The flux measured appears to be quite constant, which supports the idea that the signal is due to the ISW effect induced by structures. In the remainder of this section, we therefore apply our analysis only to the SMICA CMB map.

5.3. Discussion and alternative catalogues

It should be remembered that although the GR08 structures are considered to be good tracers of the cosmic matter distribution on scales larger than $10 h^{-1}$ Mpc, they are also known for their sparsity at these redshifts ($z \approx 0.4$ –0.7). This sparsity could lead to biased estimates of the properties of the reconstructed voids, in particular their sizes and depths could be biased. Moreover, some of the structures overlap on the sky, which could lead to systematic effects in the stacking analysis.

We thus turn to other samples, for example the catalogue of Pan et al. (2012), introduced in Sect. 2.2.4. The 1054 statistically significant voids it contains are larger than $10 h^{-1}$ Mpc in radius and, with redshifts lower than 0.1, they are much closer to us than the structures of GR08. Direct stacking gives only a weak signal at about the 1σ level, which is difficult to reconcile with the previous results. This may be due to the inclusion of a large number of small voids that could dilute the signal. Also, unlike the voids of GR08, the voids of Pan et al. (2012) have a large scatter in angular sizes on the sky, from about 2° to 20° (e.g., Ilić et al. 2013). In order to try to enhance the signal, we repeated the stacking after rescaling the voids to their effective sizes. We also subdivided the catalogue into sub-samples based on redshift, radius, and/or angular size. However, none of these attempts yielded any statistically significant result, in agreement with Ilić et al. (2013).

Finally, we applied our procedure to the catalogue of voids published by Sutter et al. (2012). These cover a rather extended range of angular scales (about 2 – 10°), and so we rescaled all the CMB patches by the effective radius of each void. Stacking subsample by subsample (*dim1*, *dim2*, *bright1*, *bright2*, *lrgdim*, *lrbright*), does not yield any significant signal. Similarly, when stacked together, the entire catalogue does not yield an ISW detection. However, since the ISW signal is expected to be stronger for the largest and closest voids (e.g., Flender et al. 2013) we tried starting from the largest void and adding them one by one, looking for the optimal number of voids, i.e., that for which the signal-to-noise ratio is maximal (see Fig. 10). We found that stacking 231, 589 or 936 voids gives roughly the same signal-to-noise (2.5σ , 2.0σ and 2.2σ , respectively). However, the more voids we stack, the smaller the amplitude of the photometry signal (see Fig. 9, this being about $-2.0\mu\text{K}$ for 936 voids, $-2.1\mu\text{K}$ for 589 voids and $-4.1\mu\text{K}$ for 231 voids, at an angular size of about 0.5 times the common rescaled radius). These amplitudes are lower than those found with the 50 GR08 voids, although above what is expected from numerical simulations (see e.g., Hernandez-Monteagudo & Smith 2012, for higher redshift and larger voids), but see also Cai et al. (2013).

The apparent angular size detected (about 0.5 times the effective void radius) in the photometry profile is smaller than that for the GR08 voids, but in agreement with expectations from simu-

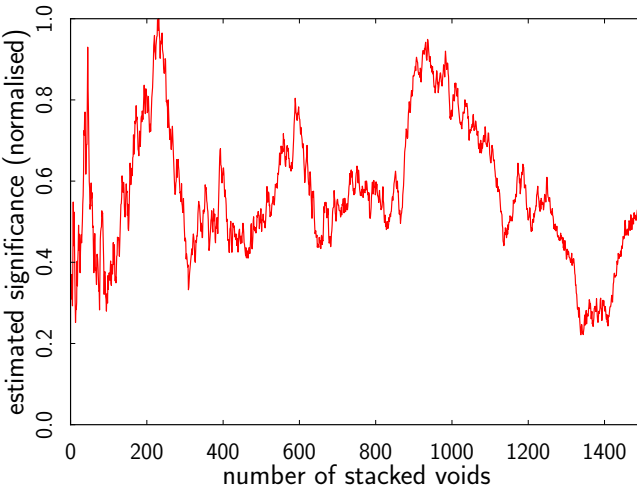


Fig. 10. Estimate of the optimal number of patches/voids to stack using the catalogue of Sutter et al. (2012). Starting from the largest void and adding one CMB patch at a time to the stack, we find at each step N the minimum of the aperture photometry profile, and we multiply this value by \sqrt{N} to find the largest signal-to-noise, assuming that the noise scales roughly as $1/\sqrt{N}$. The vertical axis has been normalized to the best signal-to-noise, obtained for 231 voids.

lations (Cai et al. 2013), and consistent with the sizes detected using WMAP data (Ilić et al. 2013).

The profiles in Fig. 9 show hints (significance about 2σ) of a positive excess below about 0.2 times the effective void radius. This may be partly because the ZOBOV algorithm uses galaxies as centres of the tessellation, meaning that the centre has to be slightly locally overdense. Fig. 9 also shows positive excess for larger apertures, partly caused by the large “hot ring” surrounding the cold feature in the stacked images, which raises the mean temperature of the stacked image for discs of radii around 0.8–1.2 times the void radius.

6. ISW map recovery

In recent years, some effort has been invested, not only to obtain the statistical cross-correlation signal between the CMB and LSS data, but also to recover a map of the ISW signal itself (Barreiro et al. 2008, 2013; Francis & Peacock 2010; Dupé et al. 2011). In particular, assuming the existence of a correlation between the CMB and the gravitational potential, it is possible to recover a map of the ISW fluctuations using a filtering method, given a tracer of the gravitational potential (e.g., the galaxy catalogues described in Sect. 2.2) and the CMB fluctuations. Given the weakness of the signal, the main objective of this section is to provide a qualitative image of the ISW fluctuations for visual inspection, and an additional consistency test of the validity of the assumed fiducial model, by comparing the statistical properties of the recovered and expected signals. In addition, this secondary anisotropy map could also be used to study the large-scale properties of the CMB, and its possible relation to some possible large-angle anomalies found in the *Planck* data (Planck Collaboration XXIII 2013).

6.1. Method

We have followed the methodology of Barreiro et al. (2008), which applies a linear filter to the CMB and to a gravitational potential tracer map, in order to reconstruct an ISW map, assuming that the cross- and auto-spectra of the signals are known. This technique has been recently applied to reconstruct the ISW map from the WMAP data and NVSS galaxy map (Barreiro et al. 2013). The filter is implemented in harmonic space and the estimated ISW map $\hat{s}_{\ell m}$ at each harmonic mode is given by (see Barreiro et al. 2008 for details)

$$\hat{s}_{\ell m} = \frac{L_{12}(\ell)}{L_{11}(\ell)} g_{\ell m} + \frac{L_{22}^2(\ell)}{L_{22}^2(\ell) + C_{\ell}^n} \left(d_{\ell m} - \frac{L_{12}(\ell)}{L_{11}(\ell)} g_{\ell m} \right), \quad (42)$$

where $L(\ell)$ corresponds to the Cholesky decomposition of the covariance matrix between the considered tracer of the potential and the ISW signal, at each multipole, which satisfies $C(\ell) = L(\ell)L^T(\ell)$. Here $d_{\ell m}$ and $g_{\ell m}$ are the CMB data and the gravitational potential tracer map, respectively, and C_{ℓ}^n is the power spectrum of the CMB signal without including the ISW effect. If full-sky coverage is not available, the covariance matrix is obtained from the corresponding pseudo-spectra. It can be shown that the expected value of the power spectrum for the reconstructed signal is given by

$$\langle C_{\ell}^s \rangle = \frac{(C_{\ell}^{gs})^2 (|C(\ell)| + C_{\ell}^g C_{\ell}^n) + |C(\ell)|^2}{C_{\ell}^g (|C(\ell)| + C_{\ell}^g C_{\ell}^n)}, \quad (43)$$

where $|C(\ell)|$ is the determinant of the tracer-ISW covariance matrix at each multipole, and C_{ℓ}^{gs} and C_{ℓ}^g are the assumed cross-spectrum and gravitational potential tracer spectra, respectively. Note that the recovered ISW power spectrum will not contain the full ISW signal, since it can only account for the part of the ISW signal probed by the tracer being considered. It is also worth noting that in detail the expected cross-correlation depends on the assumed model. However, in practice, given the weakness of the signal, it would be difficult to distinguish between two mild variants of the standard Λ CDM model. Nevertheless this approach still provides a useful consistency check.

6.2. Results

We have applied the filter described above to two different cases: combining information from the CMB and the NVSS galaxy catalogue; and applying the filter to the CMB and the recovered lensing potential map described in 2.1.2. Results have been obtained for the four *Planck* maps, C-R, NILC, SEVEM, and SMICA. For simplicity, we show the reconstructions only for the SEVEM CMB map, since the four methods give very similar results. The resolution considered for both analyses is $N_{\text{side}} = 64$.

For the first case, we are using the *Planck* fiducial model for the CMB and cross-power spectrum, while for the NVSS map we assume the model described in Sect. 2.2.1. We also take into account the presence of Poissonian noise. We have excluded the area obtained from combining the CMB mask at $N_{\text{side}} = 64$ (described in Sect. 2.1.1) as well as the area which has not been observed by NVSS. The final mask keeps around 62% of the sky. Since the filter is constructed in harmonic space, we have used an apodized version of the mask in order to reduce the mask-induced correlations. In any case, the degradation introduced by the presence of a mask is small (Barreiro et al. 2008).

For the second case, the lensing map involved applying a high-pass filter, which removed all multipoles with $\ell < 10$. This

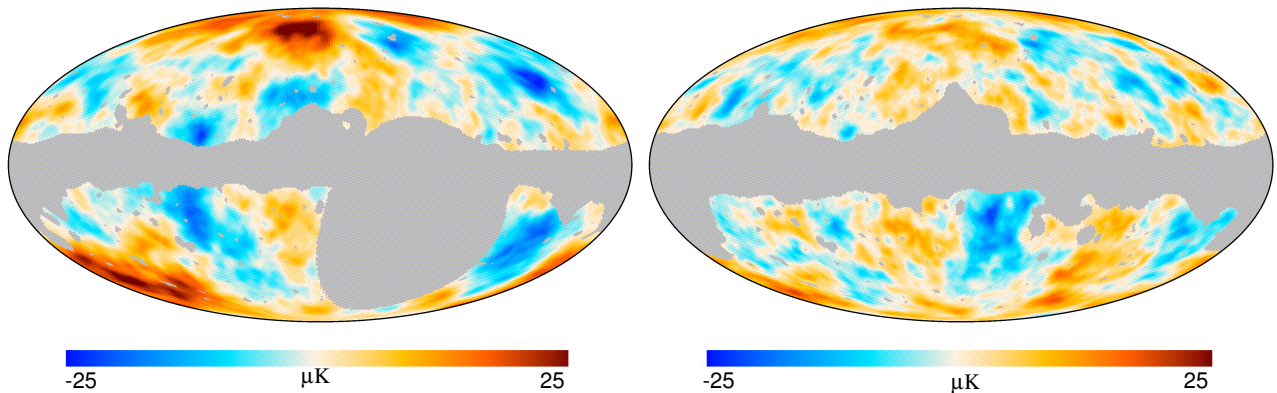


Fig. 11. Reconstructed ISW map from the *Planck* CMB and NVSS data (left) and from the *Planck* CMB and lensing potential maps (right). Note that the maps are not expected to look exactly the same, since each of them provides a partial reconstruction of the noisy ISW signal (see Sect. 6.2 for details).

filtering was done in harmonic space with the presence of a mask. To take this effect into account we used a direct estimation of the pseudo-power spectrum of these data for the power spectrum of the lensing map, after applying the corresponding apodized mask. We used the *Planck* fiducial model for the other power spectra involved, but setting to zero the cross-power for $\ell < 10$. A mask has been constructed by combining the CMB mask plus that provided for the lensing potential map (described in [Planck Collaboration XVII 2013](#)), which keeps around 67% of the sky. The corresponding apodized version of this mask was applied before reconstructing the ISW map. Note that the map given in Fig. 1 (right panel) corresponds, to a good approximation, to the first term of the right hand side of Eq. 42.

Figure 11 shows the reconstructed ISW map using the *Planck* CMB map and NVSS (left panel) and that obtained combining the CMB with the lensing potential map (right panel). There are similar structures present in both maps, but they are not expected to look exactly the same, since each of them provides only a partial reconstruction of the ISW signal. This is due to the fact that the reconstruction accounts for the part of the ISW effect probed by the considered tracer, which is different (although correlated) for each case. Moreover, due to the high-pass filter applied to the lensing potential map, the power at $\ell < 10$ for this case corresponds to the Wiener-filtered map of the CMB (to which the filter given by Eq. 42 defaults, if the cross-correlation is set to zero, as in this case), without additional information from the considered tracer.

For both cases, we have tested that the power spectrum of the recovered ISW signal, as well as that of the cross-power between the reconstructed ISW and the considered gravitational potential tracer, are consistent with the corresponding expected values. This indicates the compatibility between the assumed fiducial model and the underlying statistical properties of the data.

7. Conclusions

This paper presents the first study of the ISW effect using *Planck* data. We derived results based on three different approaches: the detection of the interplay between weak lensing of the CMB and the ISW effect, by looking at non-Gaussian signatures; the conventional cross-correlations with tracers of large-scale structure; and aperture photometry on stacks of the CMB field at the positions of known superstructures. A reconstruction of the ISW map inferred from the CMB and LSS tracers was also provided.

The correlation with lensing allows, for the first time, the detection of the ISW effect using only CMB data. This is an effective approach, because the gravitational potential responsible for deflecting CMB photons also generates ISW temperature perturbations. Using different estimators, we investigated the correlation of the *Planck* temperature map with a reconstruction of the lensing potential on the one hand, and the estimation of the ISW-lensing generated non-Gaussian signature on the other. We found that the signal strength is close to 2.5σ , for several combinations of estimator implementation and foreground-cleaned CMB maps.

We computed cross-correlations between the *Planck* CMB temperature map, and tracers of large-scale structure, namely: the NVSS survey of radio sources; and the SDSS-CMASS/LOWZ, and SDSS-MG galaxy samples. As estimators we considered the angular cross-correlation function, the angular cross-spectra, and the variance of wavelet coefficients as a function of angular scale. We performed a comparison on different component-separation maps, where we considered C-R, NILC, SEVEM, and SMICA, and found remarkable agreement between the results, indicating that the low multipoles are robustly reconstructed. Covariance matrices between the cross-correlation quantities were estimated for a set of Gaussian realizations of the CMB for the *Planck* fiducial model. For the ISW effect, we report detection significance levels of 2.9σ (NVSS), 1.7σ (SDSS-CMASS/LOWZ), and 2.0σ (SDSS-MG), which are consistent among the different estimators considered. Although these numbers are compatible with previous claims which used *WMAP* data, they are generally smaller. We believe that this discrepancy is mainly due to the different characterization of the surveys and treatment of uncertainties, since the measurement of the CMB fluctuations at the scales which contribute to the ISW detection are very similar for *Planck* and *WMAP*. Only a fraction of these differences (around 0.3σ) could be understood in terms of the different cosmological models used by each experiment – in particular, the lower values of H_0 and Ω_Λ reported by *Planck* compared with *WMAP*.

A strength of our new study lies in the fact that the amplitudes derived for the expected signals are largely consistent with unity (i.e., the model expectation), which indicates good modelling of the surveys. The CMB and LSS cross-correlation has also been tested against the null hypothesis, i.e., whether the observed signal is compatible with a null correlation. As expected for such a weak signal, there is no strong evidence of incom-

pability with the lack of correlation. In this respect, the CAPS approach seems to provide better constraints than the other estimators investigated here (CCF and the SMHWcov).

We explored the aperture photometry of stacked CMB patches at the positions of superstructures identified in the SDSS galaxy distribution. Our analysis of the Granett et al. (2008a) catalogue (50 supervoids and 50 superstructures) reproduced previous results, with similarly strong amplitude and significance levels (somewhat above and below 3σ for voids and clusters, respectively). While the most plausible source of this signal is the ISW effect associated with these structures, it shows some tension with expectations, both in terms of amplitude and scale. The same type of analysis was carried on the latest and much larger void catalogues of Sutter et al. (2012) (about 1500 voids) and Pan et al. (2012) (about 1000 voids). The results range from negligible to evidence at the 2–2.5 σ level, with a more moderate amplitude and a smaller scale, in better agreement with theoretical predictions found in the literature. The broad spectral coverage of *Planck* allows us to confirm the achromatic nature of these signals over the 44 to 353 GHz range, supporting their cosmological origin.

We reconstructed maps of the ISW effect using a linear filter, by combining the *Planck* CMB and a gravitational potential tracers. In particular, we considered both the NVSS catalogue and the reconstructed CMB lensing map as LSS tracers. Again we found good agreement between different component separation methods, as well as consistency between the expected and reconstructed auto- and cross-power spectra for the recovered ISW map.

We conclude that the ISW effect is present in *Planck* data at the level expected for Λ CDM-cosmologies, using a range of measurement methods, although there is a possible tension with the results from stacking of CMB fields centred on superstructures. Generally, our results are more conservative than previous claims using *WMAP* data, but the agreement with the expected signal is better. Future *Planck* data releases, including polarization information, as well as improved understanding of foregrounds, could improve on these results, in particular for ISW-lensing correlation and ISW-lensing map reconstruction.

Acknowledgements. The development of *Planck* has been supported by: ESA; CNES and CNRS/INSU-IN2P3-INP (France); ASI, CNR, and INAF (Italy); NASA and DoE (USA); STFC and UKSA (UK); CSIC, MICINN, JA and RES (Spain); Tekes, AoF and CSC (Finland); DLR and MPG (Germany); CSA (Canada); DTU Space (Denmark); SER/SSO (Switzerland); RCN (Norway); SFI (Ireland); FCT/MCTES (Portugal); and PRACE (EU). A description of the Planck Collaboration and a list of its members, including the technical or scientific activities in which they have been involved, can be found at http://www.sciops.esa.int/index.php?project=planck&page=Planck_Collaboration. The modal and KSW bispectrum estimator analysis was performed on the COSMOS supercomputer, part of the STFC DiRAC HPC Facility. We acknowledge the computer resources, technical expertise and assistance provided by the Spanish Supercomputing Network (RES) node at Universidad de Cantabria, and the support provided by the Advanced Computing and e-Science team at IFCA.

References

- Adelman-McCarthy, J. K., Agüeros, M. A., Allam, S. S., et al. 2008, ApJS, 175, 297
- Afshordi, N. 2004, Phys. Rev. D, 70, 083536
- Afshordi, N., Loh, Y., & Strauss, M. A. 2004, Phys. Rev. D, 69, 083524
- Aihara, H., Allende Prieto, C., An, D., et al. 2011, ApJS, 193, 29
- Barreiro, R. B., Vielva, P., Hernandez-Monteagudo, C., & Martinez-Gonzalez, E. 2008, IEEE Journal of Selected Topics in Signal Processing, 2, 747
- Barreiro, R. B., Vielva, P., Marcos-Caballero, A., & Martínez-González, E. 2013, MNRAS, 430, 259
- Bielby, R., Shanks, T., Sawangwit, U., et al. 2010, MNRAS, 403, 1261
- Blake, C. & Wall, J. 2002, MNRAS, 329, L37
- Boughn, S. & Crittenden, R. 2004, Nature, 427, 45
- Boughn, S. P. & Crittenden, R. G. 2002, Physical Review Letters, 88, 021302
- Boughn, S. P. & Crittenden, R. G. 2005, New Astronomy Review, 49, 75
- Brookes, M. H., Best, P. N., Peacock, J. A., Röttgering, H. J. A., & Dunlop, J. S. 2008, MNRAS, 385, 1297
- Bucher, M., van Tent, B., & Carvalho, C. S. 2010, MNRAS, 407, 2193
- Cabré, A., Fosalba, P., Gaztañaga, E., & Manera, M. 2007, MNRAS, 381, 1347
- Cabré, A., Gaztañaga, E., Manera, M., Fosalba, P., & Castander, F. 2006, MNRAS, 372, L23
- Cai, Y.-C., Neyrinck, M. C., Szapudi, I., Cole, S., & Frenk, C. S. 2013, ArXiv e-prints 1301.6136
- Condon, J. J., Cotton, W. D., Greisen, E. W., et al. 1998, AJ, 115, 1693
- Corasaniti, P.-S., Giannantonio, T., & Melchiorri, A. 2005, Phys. Rev. D, 71, 123521
- Creminelli, P., Nicolis, A., Senatore, L., Tegmark, M., & Zaldarriaga, M. 2006, J. Cosmology Astropart. Phys., 5, 4
- Crittenden, R. G. & Turok, N. 1996, Physical Review Letters, 76, 575
- Dupé, F.-X., Rassat, A., Starck, J.-L., & Fadili, M. J. 2011, A&A, 534, A51
- Fergusson, J. R., Liguori, M., & Shellard, E. P. S. 2010, Phys. Rev. D, 82, 023502
- Flender, S., Hotchkiss, S., & Nadathur, S. 2013, Journal of Cosmology and Astroparticle Physics, 2013, 013
- Fosalba, P. & Gaztañaga, E. 2004, MNRAS, 350, L37
- Fosalba, P., Gaztañaga, E., & Castander, F. J. 2003, ApJ, 597, L89
- Francis, C. L. & Peacock, J. A. 2009, ArXiv e-prints 0909.2494
- Francis, C. L. & Peacock, J. A. 2010, MNRAS, 406, 14
- Gaztañaga, E., Manera, M., & Multamäki, T. 2006, MNRAS, 365, 171
- Giannantonio, T., Crittenden, R., Nichol, R., & Ross, A. J. 2012, MNRAS, 426, 2581
- Giannantonio, T., Crittenden, R. G., Nichol, R. C., et al. 2006, Phys. Rev. D, 74, 063520
- Giannantonio, T., Scranton, R., Crittenden, R. G., et al. 2008, Phys. Rev. D, 77, 123520
- Giovanni, F. & Baccigalupi, C. 2005, in IAU Symposium, Vol. 225, Gravitational Lensing Impact on Cosmology, ed. Y. Mellier & G. Meylan, 117–122
- Giovanni, F., Baccigalupi, C., & Perrotta, F. 2003, Phys. Rev. D, 68, 123002
- Goldberg, D. M. & Spergel, D. N. 1999, Phys. Rev. D, 59, 103002
- Górski, K. M., Hivon, E., Banday, A. J., et al. 2005, ApJ, 622, 759
- Granett, B. R., Neyrinck, M. C., & Szapudi, I. 2008a, ApJ, 683, L99
- Granett, B. R., Neyrinck, M. C., & Szapudi, I. 2008b, ArXiv e-prints 0805.2974
- Granett, B. R., Neyrinck, M. C., & Szapudi, I. 2009, ApJ, 701, 414
- Gruppuso, A., de Rosa, A., Cabella, P., et al. 2009, MNRAS, 400, 463
- Hanson, D., Challinor, A., & Lewis, A. 2010, General Relativity and Gravitation, 42, 2197
- Hanson, D., Smith, K. M., Challinor, A., & Liguori, M. 2009, Phys. Rev. D, 80, 083004
- Hernández-Monteagudo, C. 2008, A&A, 490, 15
- Hernández-Monteagudo, C. 2010, A&A, 520, A101
- Hernández-Monteagudo, C., Ross, A., Cuesta, A., et al. 2013, ArXiv e-prints Hernandez-Monteagudo, C. & Smith, R. E. 2012, ArXiv e-prints 1212.1174
- Hinshaw, G., Spergel, D. N., Verde, L., et al. 2003, ApJS, 148, 135
- Hivon, E., Górski, K. M., Netterfield, C. B., et al. 2002, ApJ, 567, 2
- Ho, S., Cuesta, A., Seo, H.-J., et al. 2012, ArXiv e-prints 1201.2137
- Ho, S., Hirata, C., Padmanabhan, N., Seljak, U., & Bahcall, N. 2008, Phys. Rev. D, 78, 043519
- Hoyle, F. & Vogeley, M. S. 2002, ApJ, 566, 641
- Hu, W. 2000, Phys. Rev. D, 62, 043007
- Hu, W. 2002, Phys. Rev. D, 65, 023003
- Hu, W. & Okamoto, T. 2002, ApJ, 574, 566
- Hu, W. & Sugiyama, N. 1994, Phys. Rev. D, 50, 627
- Hunt, P. & Sarkar, S. 2010, MNRAS, 401, 547
- Ilić, S., Langer, M., & Douspis, M. 2013, arXiv:1301.5849
- Kamionkowski, M. & Spergel, D. N. 1994, ApJ, 432, 7
- Komatsu, E., Spergel, D. N., & Wandelt, B. D. 2005, ApJ, 634, 14
- Komatsu, E., Spergel, D. N., & Wandelt, B. D. 2005, Astrophys.J., 634, 14
- Larson, D., Dunkley, J., Hinshaw, G., et al. 2011, ApJS, 192, 16
- Lewis, A. & Challinor, A. 2006, Phys. Rep., 429, 1
- Lewis, A., Challinor, A., & Hanson, D. 2011, J. Cosmology Astropart. Phys., 3, 18
- Li, H. & Xia, J. 2010, J. Cosmology Astropart. Phys., 4, 26
- López-Corredoira, M., Sylos Labini, F., & Betancort-Rijo, J. 2010, A&A, 513, A3
- Mangilli, A. & Verde, L. 2009, Phys. Rev. D, 80, 123007
- Mangilli, A., Wandelt, B., Elsner, F., & Liguori, M. 2013
- Marcos-Caballero et al. 2013, in preparation
- Martínez-González, E., Gallegos, J. E., Argüeso, F., Cayón, L., & Sanz, J. L. 2002, MNRAS, 336, 22
- Massardi, M., Bonaldi, A., Negrello, M., et al. 2010, MNRAS, 404, 532

- McEwen, J. D., Vielva, P., Hobson, M. P., Martínez-González, E., & Lasenby, A. N. 2007, MNRAS, 376, 1211
- McEwen, J. D., Wiaux, Y., Hobson, M. P., Vandergheynst, P., & Lasenby, A. N. 2008, MNRAS, 384, 1289
- Munshi, D. & Heavens, A. 2010, Mon.Not.Roy.Astron.Soc., 401, 2406
- Neyrinck, M. C. 2008, MNRAS, 386, 2101
- Neyrinck, M. C., Gnedin, N. Y., & Hamilton, A. J. S. 2005, MNRAS, 356, 1222
- Nolta, M. R., Wright, E. L., Page, L., et al. 2004, ApJ, 608, 10
- Okamoto, T. & Hu, W. 2003, Phys. Rev. D, 67, 083002
- Paci, F., Gruppuso, A., Finelli, F., et al. 2013, ArXiv e-prints 1301.5195
- Padmanabhan, N., Hirata, C. M., Seljak, U., et al. 2005, Phys. Rev. D, 72, 043525
- Pan, D. C., Vogeley, M. S., Hoyle, F., Choi, Y.-Y., & Park, C. 2012, MNRAS, 421, 926
- Pápai, P. & Szapudi, I. 2010, ArXiv e-prints 1009.0754
- Parejko, J. K., Sunayama, T., Padmanabhan, N., et al. 2013, MNRAS, 429, 98
- Pietrobon, D., Balbi, A., & Marinucci, D. 2006a, arXiv:astro-ph/0611797
- Pietrobon, D., Balbi, A., & Marinucci, D. 2006b, Phys. Rev. D, 74, 043524
- Planck Collaboration I. 2013, Submitted to A&A
- Planck Collaboration XII. 2013, Submitted to A&A
- Planck Collaboration XV. 2013, Submitted to A&A
- Planck Collaboration XVI. 2013, Submitted to A&A
- Planck Collaboration XVII. 2013, Submitted to A&A
- Planck Collaboration XXIII. 2013, Submitted to A&A
- Planck Collaboration XXIV. 2013, Submitted to A&A
- Raccanelli, A., Bonaldi, A., Negrello, M., et al. 2008, MNRAS, 386, 2161
- Rassat, A., Land, K., Lahav, O., & Abdalla, F. B. 2006, arXiv:astro-ph/0610911
- Rees, M. J. & Sciama, D. W. 1968, Nature, 217, 511
- Regan, D., Mukherjee, P., & Seery, D. 2013, ArXiv e-prints 1302.5631
- Ross, A. J., Ho, S., Cuesta, A. J., et al. 2011, MNRAS, 417, 1350
- Sachs, R. K. & Wolfe, A. M. 1967, ApJ, 147, 73
- Sawangwit, U., Shanks, T., Cannon, R. D., et al. 2010, MNRAS, 402, 2228
- Schiavon, F., Finelli, F., Gruppuso, A., et al. 2012, MNRAS, 427, 3044
- Schlegel, D. J., Finkbeiner, D. P., & Davis, M. 1998, ApJ, 500, 525
- Scranton, R., Connolly, A. J., Nichol, R. C., et al. 2003, ArXiv:astro-ph/0307335
- Seljak, U. & Zaldarriaga, M. 1999, Phys. Rev. D, 60, 043504
- Serra, P. & Cooray, A. 2008, Phys. Rev. D, 77, 107305
- Sheth, R. K. & Tormen, G. 1999, MNRAS, 308, 119
- Smith, K. M. & Zaldarriaga, M. 2011, MNRAS, 417, 2
- Sutter, P. M., Lavaux, G., Wandelt, B. D., & Weinberg, D. H. 2012, arXiv e-prints 1207.2524
- Tegmark, M. 1997, Phys. Rev. D, 55, 5895
- Tegmark, M. & de Oliveira-Costa, A. 2001, Phys. Rev. D, 64, 063001
- Tegmark, M., Eisenstein, D. J., Strauss, M. A., et al. 2006, Phys. Rev. D, 74, 123507
- Verde, L. & Spergel, D. N. 2002, Phys. Rev. D, 65, 043007
- Vielva, P., Martínez-González, E., & Tucci, M. 2006, MNRAS, 365, 891
- Xia, J. 2009, Phys. Rev. D, 80, 103514
- Xia, J.-Q., Baccigalupi, C., Matarrese, S., Verde, L., & Viel, M. 2011, J. Cosmology Astropart. Phys., 8, 33
- Xia, J.-Q., Viel, M., Baccigalupi, C., & Matarrese, S. 2009, ArXiv e-prints 0907.4753
-
- ¹ APC, AstroParticule et Cosmologie, Université Paris Diderot, CNRS/IN2P3, CEA/Irfu, Observatoire de Paris, Sorbonne Paris Cité, 10, rue Alice Domon et Léonie Duquet, 75205 Paris Cedex 13, France
- ² Aalto University Metsähovi Radio Observatory, Metsähovintie 114, FIN-02540 Kylmälä, Finland
- ³ African Institute for Mathematical Sciences, 6-8 Melrose Road, Muizenberg, Cape Town, South Africa
- ⁴ Agenzia Spaziale Italiana Science Data Center, c/o ESRIN, via Galileo Galilei, Frascati, Italy
- ⁵ Agenzia Spaziale Italiana, Viale Liegi 26, Roma, Italy
- ⁶ Astrophysics Group, Cavendish Laboratory, University of Cambridge, J J Thomson Avenue, Cambridge CB3 0HE, U.K.
- ⁷ Astrophysics & Cosmology Research Unit, School of Mathematics, Statistics & Computer Science, University of KwaZulu-Natal, Westville Campus, Private Bag X54001, Durban 4000, South Africa
- ⁸ CITA, University of Toronto, 60 St. George St., Toronto, ON M5S 3H8, Canada
- ⁹ CNRS, IRAP, 9 Av. colonel Roche, BP 44346, F-31028 Toulouse cedex 4, France
- ¹⁰ California Institute of Technology, Pasadena, California, U.S.A.
- ¹¹ Centre for Theoretical Cosmology, DAMTP, University of Cambridge, Wilberforce Road, Cambridge CB3 0WA U.K.
- ¹² Centro de Estudios de Física del Cosmos de Aragón (CEFCA), Plaza San Juan, 1, planta 2, E-44001, Teruel, Spain
- ¹³ Computational Cosmology Center, Lawrence Berkeley National Laboratory, Berkeley, California, U.S.A.
- ¹⁴ Consejo Superior de Investigaciones Científicas (CSIC), Madrid, Spain
- ¹⁵ DSM/Irfu/SPP, CEA-Saclay, F-91191 Gif-sur-Yvette Cedex, France
- ¹⁶ DTU Space, National Space Institute, Technical University of Denmark, Elektrovej 327, DK-2800 Kgs. Lyngby, Denmark
- ¹⁷ Département de Physique Théorique, Université de Genève, 24, Quai E. Ansermet, 1211 Genève 4, Switzerland
- ¹⁸ Departamento de Física Fundamental, Facultad de Ciencias, Universidad de Salamanca, 37008 Salamanca, Spain
- ¹⁹ Departamento de Física, Universidad de Oviedo, Avda. Calvo Sotelo s/n, Oviedo, Spain
- ²⁰ Department of Astronomy and Astrophysics, University of Toronto, 50 Saint George Street, Toronto, Ontario, Canada
- ²¹ Department of Astrophysics/IMAPP, Radboud University Nijmegen, P.O. Box 9010, 6500 GL Nijmegen, The Netherlands
- ²² Department of Electrical Engineering and Computer Sciences, University of California, Berkeley, California, U.S.A.
- ²³ Department of Physics & Astronomy, University of British Columbia, 6224 Agricultural Road, Vancouver, British Columbia, Canada
- ²⁴ Department of Physics and Astronomy, Dana and David Dornsife College of Letter, Arts and Sciences, University of Southern California, Los Angeles, CA 90089, U.S.A.
- ²⁵ Department of Physics and Astronomy, University College London, London WC1E 6BT, U.K.
- ²⁶ Department of Physics, Carnegie Mellon University, 5000 Forbes Ave, Pittsburgh, PA 15213, U.S.A.
- ²⁷ Department of Physics, Gustaf Hällströminkatu 2a, University of Helsinki, Helsinki, Finland
- ²⁸ Department of Physics, Princeton University, Princeton, New Jersey, U.S.A.
- ²⁹ Department of Physics, University of California, Berkeley, California, U.S.A.
- ³⁰ Department of Physics, University of California, One Shields Avenue, Davis, California, U.S.A.
- ³¹ Department of Physics, University of California, Santa Barbara, California, U.S.A.
- ³² Department of Physics, University of Illinois at Urbana-Champaign, 1110 West Green Street, Urbana, Illinois, U.S.A.
- ³³ Dipartimento di Fisica e Astronomia G. Galilei, Università degli Studi di Padova, via Marzolo 8, 35131 Padova, Italy
- ³⁴ Dipartimento di Fisica e Scienze della Terra, Università di Ferrara, Via Saragat 1, 44122 Ferrara, Italy
- ³⁵ Dipartimento di Fisica, Università La Sapienza, P. le A. Moro 2, Roma, Italy
- ³⁶ Dipartimento di Fisica, Università degli Studi di Milano, Via Celoria, 16, Milano, Italy
- ³⁷ Dipartimento di Fisica, Università degli Studi di Trieste, via A. Valerio 2, Trieste, Italy
- ³⁸ Dipartimento di Fisica, Università di Roma Tor Vergata, Via della Ricerca Scientifica, 1, Roma, Italy
- ³⁹ Discovery Center, Niels Bohr Institute, Blegdamsvej 17, Copenhagen, Denmark
- ⁴⁰ Dpto. Astrofísica, Universidad de La Laguna (ULL), E-38206 La Laguna, Tenerife, Spain
- ⁴¹ European Space Agency, ESAC, Planck Science Office, Camino bajo del Castillo, s/n, Urbanización Villafranca del Castillo, Villanueva de la Cañada, Madrid, Spain
- ⁴² European Space Agency, ESTEC, Keplerlaan 1, 2201 AZ Noordwijk, The Netherlands
- ⁴³ Haverford College Astronomy Department, 370 Lancaster Avenue, Haverford, Pennsylvania, U.S.A.

- ⁴⁴ Helsinki Institute of Physics, Gustaf Hällströmin katu 2, University of Helsinki, Helsinki, Finland
- ⁴⁵ INAF - Osservatorio Astrofisico di Catania, Via S. Sofia 78, Catania, Italy
- ⁴⁶ INAF - Osservatorio Astronomico di Padova, Vicolo dell'Osservatorio 5, Padova, Italy
- ⁴⁷ INAF - Osservatorio Astronomico di Roma, via di Frascati 33, Monte Porzio Catone, Italy
- ⁴⁸ INAF - Osservatorio Astronomico di Trieste, Via G.B. Tiepolo 11, Trieste, Italy
- ⁴⁹ INAF/IASF Bologna, Via Gobetti 101, Bologna, Italy
- ⁵⁰ INAF/IASF Milano, Via E. Bassini 15, Milano, Italy
- ⁵¹ INFN, Sezione di Bologna, Via Irnerio 46, I-40126, Bologna, Italy
- ⁵² INFN, Sezione di Roma 1, Università di Roma Sapienza, Piazzale Aldo Moro 2, 00185, Roma, Italy
- ⁵³ INFN/National Institute for Nuclear Physics, Via Valerio 2, I-34127 Trieste, Italy
- ⁵⁴ IPAG: Institut de Planétologie et d'Astrophysique de Grenoble, Université Joseph Fourier, Grenoble 1 / CNRS-INSU, UMR 5274, Grenoble, F-38041, France
- ⁵⁵ IUCAA, Post Bag 4, Ganeshkhind, Pune University Campus, Pune 411 007, India
- ⁵⁶ Imperial College London, Astrophysics group, Blackett Laboratory, Prince Consort Road, London, SW7 2AZ, U.K.
- ⁵⁷ Infrared Processing and Analysis Center, California Institute of Technology, Pasadena, CA 91125, U.S.A.
- ⁵⁸ Institut Néel, CNRS, Université Joseph Fourier Grenoble I, 25 rue des Martyrs, Grenoble, France
- ⁵⁹ Institut Universitaire de France, 103, bd Saint-Michel, 75005, Paris, France
- ⁶⁰ Institut d'Astrophysique Spatiale, CNRS (UMR8617) Université Paris-Sud 11, Bâtiment 121, Orsay, France
- ⁶¹ Institut d'Astrophysique de Paris, CNRS (UMR7095), 98 bis Boulevard Arago, F-75014, Paris, France
- ⁶² Institut de Ciències de l'Espanya, CSIC/IEEC, Facultat de Ciències, Campus UAB, Torre C5 par-2, Bellaterra 08193, Spain
- ⁶³ Institute for Space Sciences, Bucharest-Magurale, Romania
- ⁶⁴ Institute of Astronomy and Astrophysics, Academia Sinica, Taipei, Taiwan
- ⁶⁵ Institute of Astronomy, University of Cambridge, Madingley Road, Cambridge CB3 0HA, U.K.
- ⁶⁶ Institute of Theoretical Astrophysics, University of Oslo, Blindern, Oslo, Norway
- ⁶⁷ Instituto de Astrofísica de Canarias, C/Vía Láctea s/n, La Laguna, Tenerife, Spain
- ⁶⁸ Instituto de Física de Cantabria (CSIC-Universidad de Cantabria), Avda. de los Castros s/n, Santander, Spain
- ⁶⁹ Jet Propulsion Laboratory, California Institute of Technology, 4800 Oak Grove Drive, Pasadena, California, U.S.A.
- ⁷⁰ Jodrell Bank Centre for Astrophysics, Alan Turing Building, School of Physics and Astronomy, The University of Manchester, Oxford Road, Manchester, M13 9PL, U.K.
- ⁷¹ Kavli Institute for Cosmology Cambridge, Madingley Road, Cambridge, CB3 0HA, U.K.
- ⁷² LAL, Université Paris-Sud, CNRS/IN2P3, Orsay, France
- ⁷³ LERMA, CNRS, Observatoire de Paris, 61 Avenue de l'Observatoire, Paris, France
- ⁷⁴ Laboratoire AIM, IRFU/Service d'Astrophysique - CEA/DSM - CNRS - Université Paris Diderot, Bât. 709, CEA-Saclay, F-91191 Gif-sur-Yvette Cedex, France
- ⁷⁵ Laboratoire Traitement et Communication de l'Information, CNRS (UMR 5141) and Télécom ParisTech, 46 rue Barrault F-75634 Paris Cedex 13, France
- ⁷⁶ Laboratoire de Physique Subatomique et de Cosmologie, Université Joseph Fourier Grenoble I, CNRS/IN2P3, Institut National Polytechnique de Grenoble, 53 rue des Martyrs, 38026 Grenoble cedex, France
- ⁷⁷ Laboratoire de Physique Théorique, Université Paris-Sud 11 & CNRS, Bâtiment 210, 91405 Orsay, France
- ⁷⁸ Lawrence Berkeley National Laboratory, Berkeley, California, U.S.A.
- ⁷⁹ Max-Planck-Institut für Astrophysik, Karl-Schwarzschild-Str. 1, 85741 Garching, Germany
- ⁸⁰ McGill Physics, Ernest Rutherford Physics Building, McGill University, 3600 rue University, Montréal, QC, H3A 2T8, Canada
- ⁸¹ MilliLab, VTT Technical Research Centre of Finland, Tietotie 3, Espoo, Finland
- ⁸² Niels Bohr Institute, Blegdamsvej 17, Copenhagen, Denmark
- ⁸³ Observational Cosmology, Mail Stop 367-17, California Institute of Technology, Pasadena, CA, 91125, U.S.A.
- ⁸⁴ Optical Science Laboratory, University College London, Gower Street, London, U.K.
- ⁸⁵ SB-ITP-LPPC, EPFL, CH-1015, Lausanne, Switzerland
- ⁸⁶ SISSA, Astrophysics Sector, via Bonomea 265, 34136, Trieste, Italy
- ⁸⁷ School of Physics and Astronomy, Cardiff University, Queens Buildings, The Parade, Cardiff, CF24 3AA, U.K.
- ⁸⁸ School of Physics and Astronomy, University of Nottingham, Nottingham NG7 2RD, U.K.
- ⁸⁹ Space Research Institute (IKI), Russian Academy of Sciences, Profsoyuznaya Str, 84/32, Moscow, 117997, Russia
- ⁹⁰ Space Sciences Laboratory, University of California, Berkeley, California, U.S.A.
- ⁹¹ Special Astrophysical Observatory, Russian Academy of Sciences, Nizhniy Arkhyz, Zelenchukskiy region, Karachai-Cherkessian Republic, 369167, Russia
- ⁹² Stanford University, Dept of Physics, Varian Physics Bldg, 382 Via Pueblo Mall, Stanford, California, U.S.A.
- ⁹³ Sub-Department of Astrophysics, University of Oxford, Keble Road, Oxford OX1 3RH, U.K.
- ⁹⁴ Theory Division, PH-TH, CERN, CH-1211, Geneva 23, Switzerland
- ⁹⁵ UPMC Univ Paris 06, UMR7095, 98 bis Boulevard Arago, F-75014, Paris, France
- ⁹⁶ Universität Heidelberg, Institut für Theoretische Astrophysik, Philosophenweg 12, 69120 Heidelberg, Germany
- ⁹⁷ Université de Toulouse, UPS-OMP, IRAP, F-31028 Toulouse cedex 4, France
- ⁹⁸ University Observatory, Ludwig Maximilian University of Munich, Scheinerstrasse 1, 81679 Munich, Germany
- ⁹⁹ University of Granada, Departamento de Física Teórica y del Cosmos, Facultad de Ciencias, Granada, Spain
- ¹⁰⁰ University of Miami, Knight Physics Building, 1320 Campo Sano Dr., Coral Gables, Florida, U.S.A.
- ¹⁰¹ Warsaw University Observatory, Aleje Ujazdowskie 4, 00-478 Warszawa, Poland